Alma Mater Studiorum · University of Bologna

Department of Physics and Astronomy "Augusto Righi"
Degree in Physics

Effects of rheological layering of the mantle on glacial isostatic adjustment

Supervisor:
Prof. Giorgio Spada

Submitted by:
Francesco Fonseca

Academic Year 2025/2026

Abstract

Glacial Isostatic Adjustment (GIA) is the phenomenon of flexural isostasy arising from glacial surface loads. When a mass of continental ice changes, the crust undergoes a variation in its displacement, experiencing post-glacial rebound when the ice mass is reduced and glacial isostatic depression when the mass increases. This work focuses on the latter and aims to study the effect of the inclusion of a transient rheological layer in the upper mantle.

In the chosen models, the physical parameters of the Earth follow the PREM, the viscosity of the upper mantle is 10^{21} Pa·s and the viscosity of the lower mantle is 10^{22} Pa·s. The reference model represents both the upper and lower mantle as Maxwell fluids, while the two transient models represent the upper mantle as a Burgers fluid, which can be described as a Maxwell fluid connected in series to a Kelvin-Voigt solid. In model 1 the transient viscosity (the viscosity of the Kelvin-Voigt element) is $10^{20}\,\mathrm{Pa}\cdot\mathrm{s}$, while in model 2 it is $10^{21}\,\mathrm{Pa}\cdot\mathrm{s}$.

The displacement of the Earth surface is computed using ALMA^3 (the plAnetary Love nuMbers cAlculator), an open-source Fortran program that computes the Love numbers for an axisymmetric load, and SKAL (Simulator of Kinematics from ALMA3's LLNs), a program developed as part of this thesis that computes the displacement associated with ALMA^3's Love numbers and a specific axisymmetric load function. SKAL has been developed using TABOO (a posT-glAcial reBOund calculatOr), another displacement calculator which does not support transient models, as a reference. Compared to TABOO, the ALMA^3–SKAL system consistently overestimates the radial and latitude components of the displacement by 3.5%.

The displacement was calculated using an ice mass with parabolic geometry, 15° radius, 2 km thickness and static mass $m_s = 1.079 \cdot 10^{19}$ kg. The loading process follows four different time-histories: instant loading and simple loading with durations of 1 kyr, 10 kyr, and 100 kyr. The relative displacement difference between the two transient models and the reference model has then been analysed at three reference points: the axis of the load, the top of the peripheral bulge, and a third point at 168° colatitude where the latitude displacement shows a local maximum.

At all three points, the relative displacement difference reaches its maximum value at a time that only depends on the rheological parameters and is not dependent on the time-history: at the point where the load axis meets the surface, model 1 reaches a maximum relative radial displacement difference of 15% after 200 yr, while model 2 reaches a maximum value of 7.8% after 750–900 yr; on top of the forebulge and at the third reference point, model 1 reaches a maximum relative latitude displacement difference of 45–46% after 150–200 yr, while model 2 reaches a maximum value of 20–21% after 550–650 yr.

Contents

List of Figures

List of Tables

Chapter 1

Introduction

Similarly to other branches of natural Science, the study of the Earth as a physical system can be traced back to ancient Greece. Sicilian philosopher Empedocles was the first, in the 5th century BCE, to theorize the presence of a layer of magma under a solid crust.

A first quantitative study about the internal structure of the Earth was made by Newton, in parts I and II of his *Principia Mathematica*, who assumed a homogeneous distribution of mass to compute the flattening of our planet. To do so, he also assumed a fluid-like behaviour. The fluid nature of the mantle became even more relevant in Airy's and Pratt's independent studies on isostasy, both published in 1855, which assumed that the crust behaves like a raft floating on a denser fluid material. However, this idea had to be questioned in 1863, after Kelvin's findings about the periodic tidal deformations of the earth, which could be well described by a fully elastic model. In a different study published in the same year, Kelvin settled for a model which included a rigid crust, a fluid upper mantle, and an elastic interior.

Kelvin's hypothesis is closer to our current models, but it was still proven wrong when propagation of seismic shear waves was observed throughout the mantle. This led to the use of viscoelastic models [Karato 2010].

Information about the rheology of the inner layers of the Earth can be inferred in different ways, for example by analysing the response to surface loads or by measures on the energy loss of seismic waves. The simplest viscoelastic models are Maxwell and Kelvin-Voigt bodies (which will be described in Sections 2.3 and 2.4).

The Kelvin-Voigt model can be ruled out because of the behaviour of the layers on different timescales: during seismic and tidal events, the mantle behaves as a solid, allowing for the propagation of shear waves and harmonic deformations; on longer timescales, however, the mantle behaves as a viscous fluid, for example by experiencing convection. Kelvin-Voigt bodies can be considered as solids on long timescales, while the viscous behaviour is more evident for short-term deformations; conversely, Maxwell bodies behave as elastic solids on short timescales and as fluids in the long term. This consideration alone suggests that a Maxwell fluid can be a good model of the behaviour of the mantle, at least as a first order approximation.

However, estimates of mantle viscosities show great variability, often depending on the timescale of the specific analysed phenomenon. This led to the introduction of transient rheological models. There are various possible approaches to model a transient creep behaviour, for example by introducing time-dependent viscosities in an otherwise normal Maxwell body [Peltier et al. 1980], or by using inherently transient rheological models. These can be linear, like the Burgers model or the generalized Maxwell material (which, as will be shown in Section 2.5, are two equivalent formulations of the same rheology), or non-linear models, like the Andrade rheology [Boughanemi and Mémin 2024]. Another possible strategy involves the use of a more stratified upper mantle with low viscosity layers under the lithosphere [Pan et al. 2024].

This work will focus on the effects of an inherently transient Burgers layer situated in the upper mantle, an approach that has already been successfully used in modelling post-seismic deformations [Pollitz 2003]. The model will be applied to the analysis of surface loads, and in particular to glacial isostasy.

Glacial isostasy (GIA, Glacial Isostatic Adjustment) is a term that refers to two distinct phenomena: post-glacial rebound and glacial isostatic depression. The former occurs due to the removal of surface loads, causing the rise of the underlying land masses; the letter, conversely, refers to the sinking of the crust caused by continental glaciation [Whitehouse 2018]. Since the great ice sheets are currently melting, many studies are currently focused on post-glacial rebound. This work, however, is intended as a theoretical study on the effects of transient rheologies in glacial isostatic depression.

In contrast to the lower layers, the lithosphere is well described as an elastic solid. As a consequence, GIA belongs to a broader family of phenomena called flexural isostasy. In flexural isostasy, the load compensation is not purely hydrostatic, as it would be in Pratt or Airy isostasy, but it is also due to the elastic deformation of the lithosphere. A recognizable effect of flexural isostasy is the presence of a forebulge, an elevated peripheral region where the stress under the load is compensated, as shown in Figure 1.1 [Brandes et al. 2025]. The forebulge is a recognizable geographical feature, and the time of its formation can yield information about the rheology of the underlying mantle.

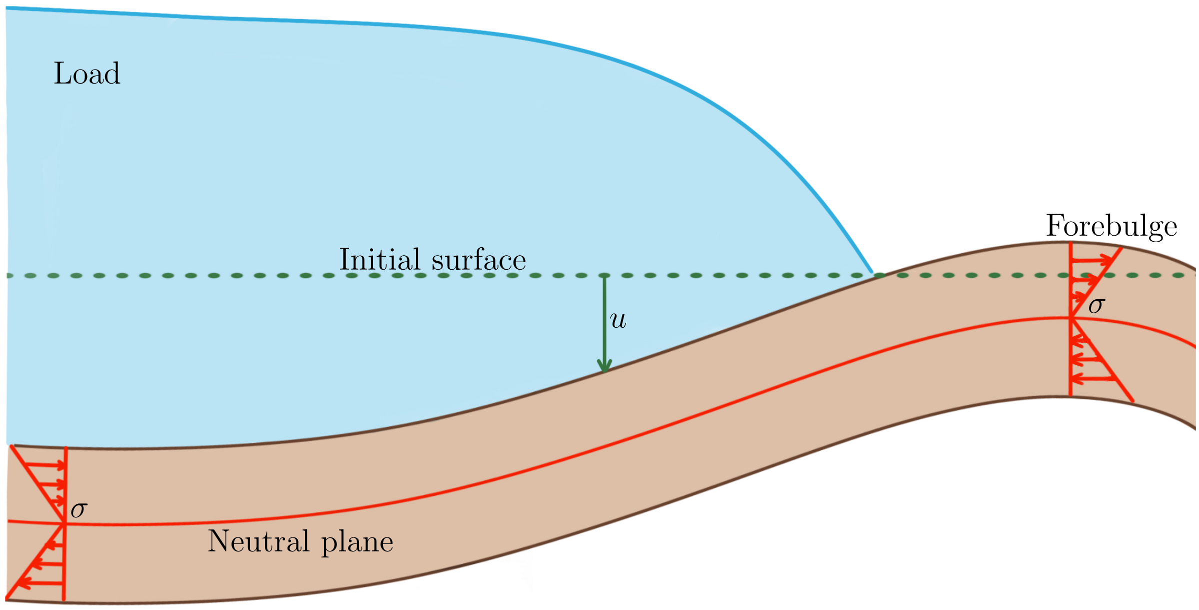

Figure 1.1: Schematic representation of flexural isostasy under the effect of a surface load. Under the load, where the surface shows downward flexure (with displacement u), the upper lithosphere is subjected to compressive stress and the lower lithosphere is subjected to extensional stress, with a neutral plane where the stress is zero. In the forebulge, where the lithosphere shows upward flexure, the opposite happens: the lower portion is subjected to compressive stress and the upper portion is subjected to extensional stress. *Drawing by Mila Casali.*

Chapter 2

Rheological models

Rheology is a branch of continuum mechanics that aims to characterise the flow of materials. In practice, this can be achieved by determining the constitutive equation of the material.

A constitutive equation is a mathematical relation that models the behaviour of a material under a certain type of external stimulus. For the scope of this thesis, constitutive relations link the stress tensor and its derivatives with the shear tensor and its derivatives:

$$f(\sigma, \dot{\sigma}, \ddot{\sigma}, \cdots) = g(\varepsilon, \dot{\varepsilon}, \ddot{\varepsilon}, \cdots)\,. \tag{2.1}$$

When functions f and g are linear compositions, the inferred behaviour is a linear rheology.

It is often important to determine the behaviour of a material on different timescales. To do so, it is possible to focus on two fundamental and ideal mechanical experiments: creep tests and relaxation tests.

In a creep test, a constant stress is applied instantaneously for an indefinitely long time, as shown in Eq. (2.2), and the strain is measured:

$$\sigma(t) = \sigma_0 H(t)\,, \tag{2.2}$$

with H being the Heaviside step function.

In a relaxation test, on the other hand, a constant strain is applied instantly, as shown in Eq. (2.3), and the stress is measured:

$$\varepsilon(t) = \varepsilon_0 H(t)\,. \tag{2.3}$$

2.1 Hooke

Linear elasticity is a mathematical model that describes materials in which infinitesimal deformations and stresses are tied by a linear combination:

$$\sigma_{ij} = C^E_{ijkl}\varepsilon_{kl} \,. \tag{2.4}$$

Eq. (2.4) is a generalization of Hooke's law of elasticity for continuum mechanics. For this reason, linear elastic materials are also called Hookean solids. In general, the elasticity tensor C^E_{ijkl} has at most 21 independent components, which reduce to two for isotropic materials. A linear equation linking the stress and strain tensors can be written using any pair of different elastic moduli. In this work, the shear modulus and the bulk modulus, defined in Eqs. (2.5) and (2.6), respectively, are used:

$$\mu = \frac{\sigma_{ij} - \frac{1}{3}\sigma_{kk}\delta_{ij}}{2\left(\varepsilon_{ij} - \frac{1}{3}\varepsilon_{kk}\delta_{ij}\right)} = \frac{\tau_{ij}}{\gamma_{ij}} \,, \tag{2.5}$$

with $\tau_{ij} = \sigma_{ij} - \frac{1}{3}\sigma_{kk}\delta_{ij}$ and $\gamma_{ij} = 2\left(\varepsilon_{ij} - \frac{1}{3}\varepsilon_{kk}\delta_{ij}\right)$ being the deviatoric components of the stress and shear tensors, respectively; and

$$K = -V\frac{dp}{dV} = \frac{\sigma_{ii}}{3\varepsilon_{jj}} \,. \tag{2.6}$$

Thus, the constitutive equation for an isotropic Hookean solid becomes

$$\sigma_{ij} = 2\mu\left(\varepsilon_{ij} - \frac{1}{3}\varepsilon_{kk}\delta_{ij}\right) + K\varepsilon_{kk}\delta_{ij} \,. \tag{2.7}$$

A more compact symbolic equation for linear elastic materials is the following:

$$\sigma = E\varepsilon \,, \tag{2.8}$$

with E being a generic elastic modulus. From now on, the former Eq. (2.8) will be used, if not stated otherwise. The response of an elastic solid to creep and relaxation tests (see Eqs. (2.2) and (2.3)) is expressed by Eqs. (2.9) and (2.10), respectively.

$$\varepsilon(t) = \frac{\sigma_0}{E}H(t) \,, \tag{2.9}$$

$$\sigma(t) = E\varepsilon_0 H(t) \,. \tag{2.10}$$

In rheological diagrams, a linear elastic component is represented by a spring.

2.2 Newton

Newtonian fluids are materials in which stress is linearly correlated to the strain rate, as expressed by Eq. (2.11):

$$\sigma_{ij} = -p\delta_{ij} + C^V_{ijkl}\dot{\varepsilon}_{kl}\,, \tag{2.11}$$

where p is the thermodynamic pressure. The viscosity tensor C^V_{ijkl}, similar to the elasticity tensor used in Eq. (2.4), can be defined by at most 21 independent parameters, but the behaviour of isotropic fluids can be uniquely determined using the shear and bulk viscosity defined in Eqs. (2.12) and (2.13), respectively:

$$\eta = \frac{\sigma_{ij} - \frac{1}{3}\sigma_{kk}\delta_{ij}}{2\left(\dot{\varepsilon}_{ij} - \frac{1}{3}\dot{\varepsilon}_{kk}\delta_{ij}\right)} = \frac{\tau_{ij}}{\dot{\gamma}_{ij}}\,, \tag{2.12}$$

with $\tau_{ij} = \sigma_{ij} - \frac{1}{3}\sigma_{kk}\delta_{ij}$ and $\dot{\gamma}_{ij} = 2\left(\dot{\varepsilon}_{ij} - \frac{1}{3}\dot{\varepsilon}_{kk}\delta_{ij}\right)$ being the deviatoric components of the stress and shear rate tensors, respectively; and

$$\zeta = \frac{\sigma_{ii} + 3p}{3\dot{\varepsilon}_{jj}}\,. \tag{2.13}$$

The general constitutive equation for an isotropic Newtonian fluid thus becomes

$$\sigma_{ij} = -p\delta_{ij} + 2\eta\left(\dot{\varepsilon}_{ij} - \frac{1}{3}\dot{\varepsilon}_{kk}\delta_{ij}\right) + \zeta\dot{\varepsilon}_{kk}\delta_{ij}\,. \tag{2.14}$$

When the viscosity tensor is null or negligible, the stress of the fluid equals its thermodynamic pressure and has no deviatoric components. Such a fluid is incompressible and inviscid, and is thus called an inviscid fluid.

Since the phenomena analysed in this work only involve shearing deformations, it is possible to use the following constitutive equation:

$$\sigma = \eta\dot{\varepsilon}\,. \tag{2.15}$$

The response of Newtonian fluids to creep and relaxation tests (Eqs. (2.2), (2.3)) is thus expressed by Eqs. (2.16) and (2.17), respectively.

$$\varepsilon(t) = \frac{\sigma_0}{\eta}tH(t)\,, \tag{2.16}$$

$$\sigma(t) = \eta\varepsilon_0\delta(t)\,, \tag{2.17}$$

where δ is the Dirac delta. In rheological diagrams, a Newtonian component is represented by a dashpot.

2.3 Maxwell

Many materials exhibit viscoelastic behaviour, which means that they have both viscous and elastic properties. One of the simplest viscoelastic materials is the Maxwell fluid, a model represented by a Newtonian and a Hookean element connected in series.

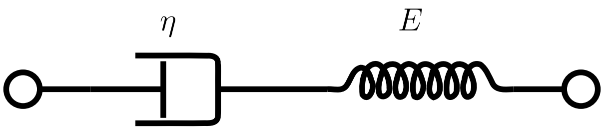

Figure 2.1: Maxwell model.

Since the strain rate of two bodies connected in series is given by the sum of the single bodies' strain rates, while the two are subjected to the same stress, the constitutive equation of a Maxwell fluid is the following:

$$\frac{\dot{\sigma}}{E} + \frac{\sigma}{\eta} = \dot{\varepsilon}\,. \tag{2.18}$$

During a creep test (Eq. (2.2)), the material exhibits an instantaneous deformation, due to the elastic component, followed by a linear strain, caused by the Newtonian element. This is expressed by Eq. (2.19). Since the deformation is not completely reversible, the material behaves as a fluid. However, for high viscosity and short timescales, the permanent deformation is negligible when compared to the elastic behaviour.

$$\varepsilon(t) = \left(\frac{\sigma_0}{E} + \frac{\sigma_0}{\eta}t\right) H(t)\,. \tag{2.19}$$

A Maxwell fluid is thus an ideal model for the representation of the mantle, since it is able to mediate shear waves while being subject to convective movement on longer timescales.

During relaxation experiments (Eq. (2.3)), Maxwell fluids exhibit exponential relaxation, as shown in Eq. (2.20), which means that the internal energy is dissipated due to the viscous component:

$$\sigma(t) = E\varepsilon_0 e^{-\frac{t}{\tau}} H(t)\,, \tag{2.20}$$

with $\tau = \frac{\eta}{E}$ being the relaxation time.

2.4 Kelvin-Voigt

Another possible way to combine viscous and elastic behaviour is by connecting a Newtonian and Hookean element in parallel, obtaining a Kelvin-Voigt body.

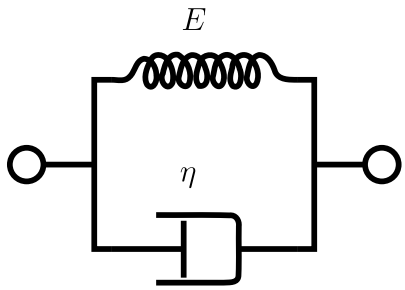

Figure 2.2: Kelvin-Voigt model.

To determine the constitutive equation of this material, it is sufficient to observe that two elements connected in parallel are subjected to the same strain, while the stress of the system is the sum of the stresses of the single elements. Thus, the behaviour of a Kelvin-Voigt material is expressed by the following relation:

$$\sigma = E\varepsilon + \eta\dot{\varepsilon}\,. \tag{2.21}$$

When it undergoes a creep test (Eq. (2.2)), the material exhibits an initial transient phase followed by an indefinitely long phase of constant strain, as expressed by Eq. (2.22):

$$\varepsilon(t) = \frac{\sigma_0}{E}\left(1 - e^{-\frac{t}{\tau}}\right) H(t)\,, \tag{2.22}$$

with $\tau = \frac{\eta}{E}$ being the retardation time.

The dominant long-term behaviour of the material is elastic; for this reason, it is also called a Kelvin-Voigt solid.

Under relaxation test conditions (Eq. (2.3)), Kelvin-Voigt materials behave as elastic solids, with only an initial spike in stress due to the viscous component, expressed by a Dirac delta in Eq. (2.23):

$$\sigma(t) = E\varepsilon_0 H(t) + \eta\varepsilon_0\delta(t)\,. \tag{2.23}$$

2.5 Burgers

Sometimes, it is necessary to model a material that exhibits both relaxation and transient behaviour. There are two ways to obtain such a material.

The first method involves a Maxwell fluid and a Kelvin-Voigt solid connected in series, as shown in Figure 2.3. The constitutive equation of this model can be obtained using the sum of the first and second derivatives of the strain of the two elements and is the following:

$$\sigma + \left(\frac{\eta_1}{E_1} + \frac{\eta_2}{E_1} + \frac{\eta_2}{E_2}\right)\dot{\sigma} + \frac{\eta_1\eta_2}{E_1E_2}\ddot{\sigma} = \eta_2\dot{\varepsilon} + \frac{\eta_1\eta_2}{E_1}\ddot{\varepsilon}\,. \tag{2.24}$$

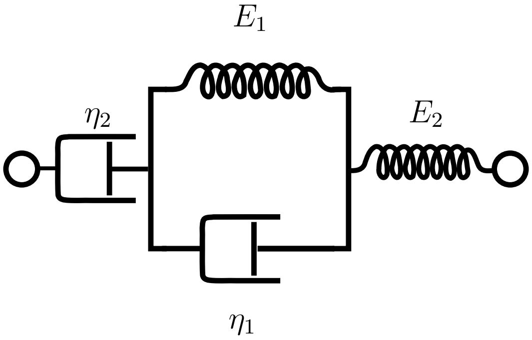

Figure 2.3: Burgers model as Kelvin-Voigt and Maxwell in series.

The second way to model a transient and relaxing material is by using a two-branch generalized Maxwell model, shown in Figure 2.4.

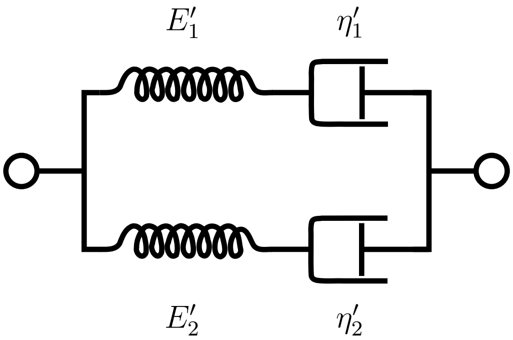

Figure 2.4: Burgers model as a generalized Maxwell.

The constitutive equation for this model can be obtained using the method shown in appendix A, and it is the following:

$$\sigma + \left(\frac{\eta'_1}{E'_1} + \frac{\eta'_2}{E'_2}\right)\dot{\sigma} + \frac{\eta'_1\eta'_2}{E'_1E'_2}\ddot{\sigma} = \left(\eta'_1 + \eta'_2\right)\dot{\varepsilon} + \frac{\eta'_1\eta'_2\left(E'_1 + E'_2\right)}{E'_1E'_2}\ddot{\varepsilon}\,. \tag{2.25}$$

Since both representations yield a constitutive equation of the form

$$\sigma + q_1\dot{\sigma} + q_2\ddot{\sigma} = p_1\dot{\varepsilon} + p_2\ddot{\varepsilon}\,, \tag{2.26}$$

an appropriate choice of parameters E'_1, E'_2, η'_1 and η'_2 will provide a generalized Maxwell representation completely equivalent to the Kelvin-Voigt representation, and vice versa [Müller 1986].

The equations that link the parameters used in Eqs. (2.24) and (2.25) can be obtained by solving the following system:

$$\begin{cases} \dfrac{\eta_1'}{E_1'} + \dfrac{\eta_2'}{E_2'} = \dfrac{\eta_1}{E_1} + \dfrac{\eta_2}{E_1} + \dfrac{\eta_2}{E_2} \\ \dfrac{\eta_1'\eta_2'}{E_1'E_2'} = \dfrac{\eta_1\eta_2}{E_1E_2} \\ \eta_1' + \eta_2' = \eta_2 \\ \dfrac{\eta_1'\eta_2'\left(E_1' + E_2'\right)}{E_1'E_2'} = \dfrac{\eta_1\eta_2}{E_1} \end{cases} . \tag{2.27}$$

The solution of the system yields the following equations:

$$\begin{Bmatrix} E' \\ \eta' \end{Bmatrix}_i = \frac{1}{2}\begin{Bmatrix} E_2 \\ \eta_2 \end{Bmatrix}\left[1 \pm \frac{1}{\sqrt{\Delta}}\left(\frac{\eta_2}{E_2} - \frac{\eta_1}{E_1} + \begin{Bmatrix} -1 \\ +1 \end{Bmatrix}\frac{\eta_2}{E_1}\right)\right], \tag{2.28}$$

with $i = 1, 2$ and

$$\Delta = \left(\frac{\eta_1}{E_1} + \frac{\eta_2}{E_1} + \frac{\eta_2}{E_2}\right)^2 - 4\frac{\eta_1\eta_2}{E_1E_2} . \tag{2.29}$$

And, conversely,

$$\begin{cases} E_1 = \dfrac{E_1'E_2'\left(E_1' + E_2'\right)\left(\eta_1' + \eta_2'\right)^2}{\left(\eta_1'E_2' - \eta_2'E_1'\right)^2} \\ E_2 = E_1' + E_2' \\ \eta_1 = \dfrac{\eta_1'\eta_2'\left(\eta_1' + \eta_2'\right)\left(E_1' + E_2'\right)^2}{\left(\eta_1'E_2' - \eta_2'E_1'\right)^2} \\ \eta_2 = \eta_1' + \eta_2' \end{cases} . \tag{2.30}$$

This is a special case of a more general theorem that states the equivalence of a series of Kelvin-Voigt elements and a parallel of Maxwell elements [Tschoegl 1989].

The response of the material to a creep test (Eq. (2.2)) can be easily determined using the constitutive equation Eq. (2.24), referred to the series model shown in Figure 2.3. Since the total strain for a series of rheological bodies is the sum of the strains of the components, the creep response is the following:

$$\varepsilon(t) = \left[\frac{\sigma_0}{E_2} + \frac{\sigma_0}{\eta_2}t + \frac{\sigma_0}{E_1}\left(1 - e^{-\frac{t}{\tau_{ret}}}\right)\right]H(t), \tag{2.31}$$

with $\tau_{ret} = \frac{\eta_1}{E_1}$ being the retardation time. It is easy to see that the three terms of the function are the creep responses of, respectively, a linear elastic material, a Newtonian viscous fluid, and a Kelvin-Voigt solid. The Burgers fluid inherits its transient characteristics from the latter.

When the relaxation behaviour of the material is tested (Eq. (2.3)), it is more convenient to use constitutive equation Eq. (2.25), which arises from two Maxwell fluids connected in parallel, as shown in Figure 2.4. The total stress of two rheological bodies connected in parallel is the sum of the stresses of the single elements. Thus, the relaxation response of a Burgers body is the following:

$$\sigma(t) = \varepsilon_0 \left(E_1' e^{-\frac{t}{\tau_1}} + E_2' e^{-\frac{t}{\tau_2}} \right) H(t) \,, \tag{2.32}$$

with $\tau_1 = \frac{\eta_1'}{E_1'}$ and $\tau_2 = \frac{\eta_2'}{E_2'}$ being the relaxation times of the two branches.

Chapter 3

Surface loads

The following dissertation is based upon the book *Glacial Isostatic Adjustment: Theory for a Spherically Symmetric Earth and Numerical Results* [Spada and Melini 2025].

Surface loads may be distinguished into two kinds: axisymmetric (AX loads), when they show axial symmetry, and non-axisymmetric (NAX loads), otherwise. Models standing for NAX loads can be used for AX loads, while the opposite does not always hold true.

A generic surface load can be defined by the following equation:

$$L(t, \theta, \lambda) = -\frac{1}{\gamma_0} \frac{dF_\perp}{dA}(t, \theta, \lambda)\,, \tag{3.1}$$

where $dF_\perp$ is the normal force, γ_0 is the acceleration of gravity on the surface, dA is the unit of area. In this work, only AX loads that can be factorized as shown below will be considered:

$$L(t, \theta, \lambda) = f(t)\, \sigma(\theta, \lambda)\,. \tag{3.2}$$

The function f is non-dimensional and is called the load time-history, while σ has the dimension of a surface density of mass and is called the load function.

We can now define the mass of the load. Two kinds of mass can be used: static mass and dynamic mass. The static mass of a load is a time-independent quantity defined as the integral of the load function over the surface:

$$m_s = r_\oplus^2 \int_\Omega \sigma(\theta, \lambda)\, d\Omega\,, \tag{3.3}$$

with $r_\oplus$ being the radius of the Earth. The dynamic mass is the integral of the load over the surface, and is time-dependent. It is clear that, if the load can be factorized as shown in Eq. (3.2), the dynamic mass is the product of the time-history and the static mass:

$$\mu(t) = r_\oplus^2 \int_\Omega L(t, \theta, \lambda)\, d\Omega = f(t)\, m_s\,. \tag{3.4}$$

A load with static mass $m_s = 0$ is called balanced.

3.1 Load geometry

A generic load function can always be expressed in terms of complex spherical harmonics, as described in the following equation:

$$\sigma(\theta, \lambda) = \sum_{\ell=0}^{\infty} \sum_{m=-\ell}^{\ell} \sigma_\ell^m Y_\ell^m(\theta, \lambda)\,, \tag{3.5}$$

where Y_ℓ^m is the spherical harmonic of degree ℓ and order m and the spherical harmonic coefficients are

$$\sigma_\ell^m = \int_\Omega \sigma(\theta, \lambda) Y_\ell^{m*}(\theta, \lambda)\, d\Omega\,. \tag{3.6}$$

From Eq. (3.5) and the definition of the spherical harmonics, it is possible to obtain the real harmonic expansion

$$\sigma(\theta, \lambda) = \sum_{\ell=0}^{\infty} \sum_{m=0}^{\ell} \left(c_\ell^m \cos(m\lambda) + s_\ell^m \sin(m\lambda)\right) P_\ell^m(\cos\theta)\,, \tag{3.7}$$

with P_ℓ^m being the associated Legendre polynomial of degree ℓ and order m and the coefficients defined as

$$\begin{Bmatrix} c_\ell^m \\ s_\ell^m \end{Bmatrix} = (2 - \delta_{0m}) \sqrt{\frac{2\ell + 1}{4\pi} \frac{(l-m)!}{(l+m)!}} \begin{Bmatrix} +\Re(\sigma_\ell^m) \\ -\Im(\sigma_\ell^m) \end{Bmatrix}\,. \tag{3.8}$$

By solving Eq. (3.3) using the factorised load function represented by Eq. (3.5), the static mass of a generic surface load is

$$m_s = \sqrt{4\pi} r_\oplus^2 \sigma_0^0 = 4\pi r_\oplus^2 c_0^0\,. \tag{3.9}$$

The property of axial symmetry means that it is always possible to find a frame, which can be called load reference frame (LRF), where the load can be represented by a load function σ^{AX} that only depends on the new colatitude Θ. In this frame, the axis over which $\Theta = 0$ corresponds to the axis of symmetry of the load, and the pole is the point where the axis of symmetry intersects the surface. This means that Eq. (3.7) simplifies to

$$\sigma^{AX}(\Theta) = \sum_{\ell=0}^{\infty} \sigma_\ell^{AX} P_l(\cos\Theta)\,, \tag{3.10}$$

where P_ℓ is the Legendre polynomial of degree ℓ and the coefficients are defined by the following equation.

$$\sigma_\ell^{AX} = \frac{2\ell+1}{2} \int_{-1}^{+1} \sigma^{AX}(x) P_\ell(x)\, dx\,. \tag{3.11}$$

For an AX load, Eq. (3.3) simplifies to

$$m_s^{AX} = 2\pi r_\oplus^2 \int_0^\pi \sigma^{AX}(\Theta) \sin\Theta\, d\Theta\,, \tag{3.12}$$

and the explicit form of the static mass is

$$m_s^{AX} = 4\pi r_\oplus^2 \sigma_0^{AX}\,. \tag{3.13}$$

The simplest example of AX load, which is important when studying more complex geometries, is the unit load, defined as

$$\sigma^\delta(\Theta) = \frac{m_s^\delta}{2\pi r_\oplus^2} \delta(1-\cos\Theta)\,, \tag{3.14}$$

with m_s^δ being the static mass of the unit load and δ being the Dirac delta.

The coefficients of the harmonic expansion (Eq. (3.10)) are

$$\sigma_\ell^\delta = m_s^\delta \frac{2\ell+1}{4\pi r_\oplus^2}\,. \tag{3.15}$$

3.1.1 Parabolic load

Among AX loads, the one used in this work is the parabolic load. Contrary to what the name may suggest, the cross section of this load is not a parabola. However, it is parabolic in the variable $\cos\Theta$, and it is defined by Eq. (3.16):

$$\sigma^P(\Theta) = \rho_i \begin{cases} h_0 \sqrt{\dfrac{\cos\Theta - \cos\alpha}{1-\cos\alpha}} & \text{if} \quad 0 \le \Theta \le \alpha \\ 0 & \text{if} \quad \alpha < \Theta \le \pi \end{cases}\,, \tag{3.16}$$

where ρ_i is the mass density of the material, h_0 is the thickness of the load at $\Theta = 0$ and α is the angular radius of the load. The profile of a parabolic load is shown in Figure 3.1.

The harmonic expansion of a parabolic load in the LRF is

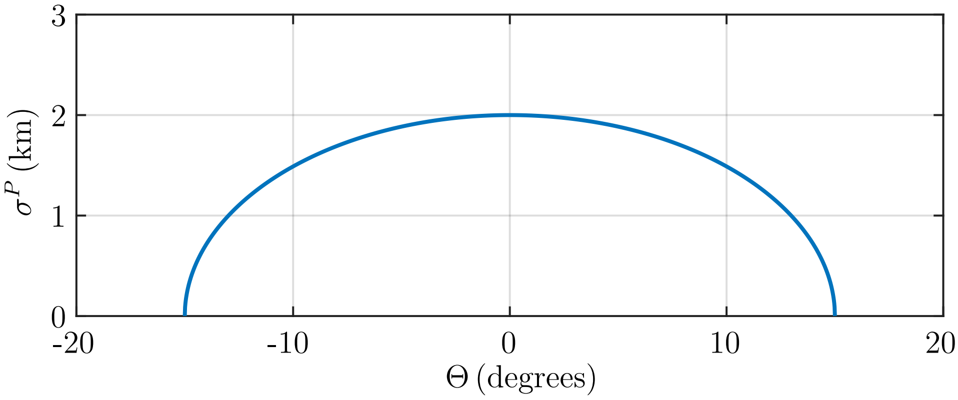

Figure 3.1: Load function of a parabolic load.

$$\sigma^P(\Theta) = \sum_{\ell=0}^{\infty} \sigma_\ell^P P_l(\cos\Theta)\,; \tag{3.17}$$

the coefficients σ_ℓ^P can be found by solving Eq. (3.11). The result is shown in the following equation:

$$\sigma_\ell^P = \frac{\rho_i h_o}{3}\,(1-\cos\alpha)\begin{cases} 1 & \text{if} \quad \ell = 0 \\ \xi_\ell(\alpha) & \text{if} \quad \ell > 0 \end{cases}, \tag{3.18}$$

where

$$\xi_\ell(\alpha) = \frac{3}{4(1-\cos\alpha)^2}\left[\frac{T_{\ell+1}(\cos\alpha) - T_{\ell+2}(\cos\alpha)}{\ell+3/2} - \frac{T_{\ell-1}(\cos\alpha) - T_\ell(\cos\alpha)}{\ell - 1/2}\right], \tag{3.19}$$

with $T_\ell(\cos\alpha) = \cos(\ell\alpha)$ being the Chebyshev polynomial of the first kind and degree ℓ.

The parabolic model, however, breaks the principle of mass conservation. Its static mass, which can be found by inserting equation 3.18 inside equation 3.13, is the following:

$$m_s^P = \frac{4}{3}\pi r_\oplus^2 \rho_i h_0\,(1-\cos\alpha)\,, \tag{3.20}$$

and thus its dynamic mass changes over time. For this reason, a balanced parabolic load can be introduced.

3.1.2 Balanced parabolic load

To balance a load, it is possible to introduce the complementary disc load, a load function with negative static mass, that is defined as follows:

$$\sigma^C(\Theta) = \rho_i \begin{cases} 0 & \text{if} \quad 0 \leq \Theta \leq \alpha \\ h' & \text{if} \quad \alpha < \Theta \leq \pi \end{cases}, \tag{3.21}$$

where h' is a negative height, the expression of which depends on the load to be complemented. The static mass of the complementary disc load is

$$m_s^C = 2\pi r_\oplus^2 \rho_i h' \left(1 + \cos\alpha\right). \tag{3.22}$$

The balanced parabolic load function is defined as the sum of a parabolic load and a complementary disc:

$$\sigma^{CP}(\Theta) = \sigma^P(\Theta) + \sigma^C(\Theta) = \rho_i \begin{cases} h_0 \sqrt{\dfrac{\cos\Theta - \cos\alpha}{1 - \cos\alpha}} & \text{if} \quad 0 \leq \Theta \leq \alpha \\ h' & \text{if} \quad \alpha < \Theta \leq \pi \end{cases}. \tag{3.23}$$

We can now determine the value of h' by imposing $m_s^{CP} = m_s^P + m_s^C = 0$, that yields the following equation:

$$h' = -\frac{2}{3}\frac{1 - \cos\alpha}{1 + \cos\alpha} h_0 \,. \tag{3.24}$$

It is now possible to express the harmonic coefficients that define the load in the LRF. The solution of Eq. (3.11) gives the following result:

$$\sigma_\ell^{CP} = \begin{cases} 0 & \text{if} \quad \ell = 0 \\ \sigma_\ell^P + \dfrac{\rho_i h'}{2}\left[P_{\ell+1}(\cos\alpha) - P_{\ell+1}(\cos\alpha)\right] & \text{if} \quad \ell > 0 \end{cases}. \tag{3.25}$$

3.2 Response to surface loads

It is now possible to determine the components of the surface displacement by considering the toroidal-poloidal decomposition of a solenoidal displacement field [Sabadini et al. 1995]. Due to the spherical symmetry of the Earth model that will be used in this work, the toroidal components can be neglected. The components of the surface displacement can thus be written as

$$\begin{Bmatrix} u_r \\ u_\theta \\ u_\lambda \end{Bmatrix} (s, r_\oplus, \theta, \lambda) = \sum_{\ell=0}^{\infty} \sum_{m=-l}^{l} \begin{Bmatrix} u_\ell^m \\ v_\ell^m \\ v_\ell^m \end{Bmatrix} (s, r_\oplus) \cdot \begin{Bmatrix} 1 \\ \partial_\theta \\ \frac{\partial_\lambda}{\sin\theta} \end{Bmatrix} Y_\ell^m(\theta, \lambda)\,, \tag{3.26}$$

where u_ℓ^m and v_ℓ^m satisfy the following constitutive equation:

$$\begin{Bmatrix} u_\ell^m \\ v_\ell^m \end{Bmatrix} (s, r_\oplus) = \begin{Bmatrix} c_\ell \\ d_\ell \end{Bmatrix} (s)\, \sigma_\ell^m \mathscr{L}\{f\}(s)\,, \tag{3.27}$$

with c_ℓ and d_ℓ being model-dependent constants and $\mathscr{L}\{f\}$ being the Laplace transform of the time-history. σ_ℓ^m are the coefficients of the harmonic decomposition of the load as defined in Eq. (3.6).

It is now possible to determine the response to an impulsive unit load, defined as follows:

$$L(t, \Theta) = \delta(t)\sigma^\delta(\Theta)\,, \tag{3.28}$$

where σ^δ is the unit load as defined in Eq. (3.14). Since $\mathscr{L}\{\delta\} = 1$, the response is

$$\begin{Bmatrix} u_\ell^m \\ v_\ell^m \end{Bmatrix}^\delta (s, r_\oplus) = \begin{Bmatrix} c_\ell \\ d_\ell \end{Bmatrix} (s)\, \sigma_\ell^\delta\,, \tag{3.29}$$

σ_ℓ^δ being the coefficients of the harmonic expansion (see Eq. (3.15)).

Using this response, it is possible to define the load Love numbers (LLNs) or load-deformation coefficients (LDCs) h_ℓ and l_ℓ in the Laplace domain:

$$\mathscr{L}\begin{Bmatrix} h_\ell \\ l_\ell \end{Bmatrix}(s) = \frac{m_\oplus}{m_s^\delta r_\oplus} \begin{Bmatrix} u_\ell \\ v_\ell \end{Bmatrix}^\delta (s, r_\oplus) = m_\oplus \frac{2\ell + 1}{4\pi r_\oplus^3} \begin{Bmatrix} c_\ell \\ d_\ell \end{Bmatrix} (s)\,, \tag{3.30}$$

with $m_\oplus$ and $r_\oplus$ being the mass and radius of the Earth, respectively, and m_s^δ being the static mass of the unit load. When returning to the time domain, it is possible to use the new numbers $\bar{h}_\ell$ and $\bar{l}_\ell$, defined as the time convolution product of the time-history and the LDCs:

$$\begin{Bmatrix} \bar{h}_\ell \\ \bar{l}_\ell \end{Bmatrix} (t) = \begin{Bmatrix} h_\ell \\ l_\ell \end{Bmatrix} (t) \otimes f(t) = \mathscr{L}\begin{Bmatrix} h_\ell \\ l_\ell \end{Bmatrix}(s)\, \mathscr{L}\{f\}(s)\,. \tag{3.31}$$

Using the former equations, Eq. (3.26) becomes:

$$\begin{Bmatrix} u_r \\ u_\theta \\ u_\lambda \end{Bmatrix} (t, r_\oplus, \theta, \lambda) = \frac{3}{\rho_\oplus} \sum_{\ell=0}^{\infty} \sum_{m=-l}^{l} \frac{\sigma_\ell^m}{2\ell + 1} \begin{Bmatrix} \bar{h}_\ell \\ \bar{l}_\ell \\ \bar{l}_\ell \end{Bmatrix} (t) \cdot \begin{Bmatrix} 1 \\ \partial_\theta \\ \frac{\partial_\lambda}{\sin\theta} \end{Bmatrix} Y_\ell^m(\theta, \lambda)\,, \tag{3.32}$$

with $\rho_\oplus = 3m_\oplus / \left(4\pi r_\oplus^3\right)$ being the average density of the Earth. Now, considering only AX loads in the LRF, the response simplifies to

$$\begin{Bmatrix} u_R \\ u_\Theta \end{Bmatrix}^{AX} (t, r_\oplus, \Theta) = \frac{3}{\rho_\oplus} \sum_{\ell=0}^{\infty} \frac{\sigma_\ell^{AX}}{2\ell + 1} \begin{Bmatrix} \bar{h}_\ell \\ \bar{l}_\ell \end{Bmatrix} (t) \cdot \begin{Bmatrix} 1 \\ \partial_\Theta \end{Bmatrix} P_\ell(\cos\Theta)\,. \tag{3.33}$$

3.2.1 Time-histories

In this work, two kinds of time histories will be used: instant loading and simple loading.

Instant loading refers to a surface load characterized by a step time-history, as shown in the following equation:

$$f^s(t) = H(t)\,, \tag{3.34}$$

with H being the Heaviside step function. This means that the Laplace transformed time-history can be expressed as:

$$\mathscr{L}\{f^s\}(s) = \frac{1}{s}\,. \tag{3.35}$$

Clearly, this is equivalent to a creep test (see Eq. (2.2)).

Simple loading, on the other hand, refers to a ramp time-history, expressed by the following equation and shown in Figure 3.2:

$$f^r(t) = H(t) - \left(1 - \frac{t}{\tau}\right)\left[H(t) - H(t-\tau)\right]. \tag{3.36}$$

Its Laplace transform is:

$$\mathscr{L}\{f^r\}(s) = \frac{1}{\tau s^2}\left(1 - e^{-\tau s}\right). \tag{3.37}$$

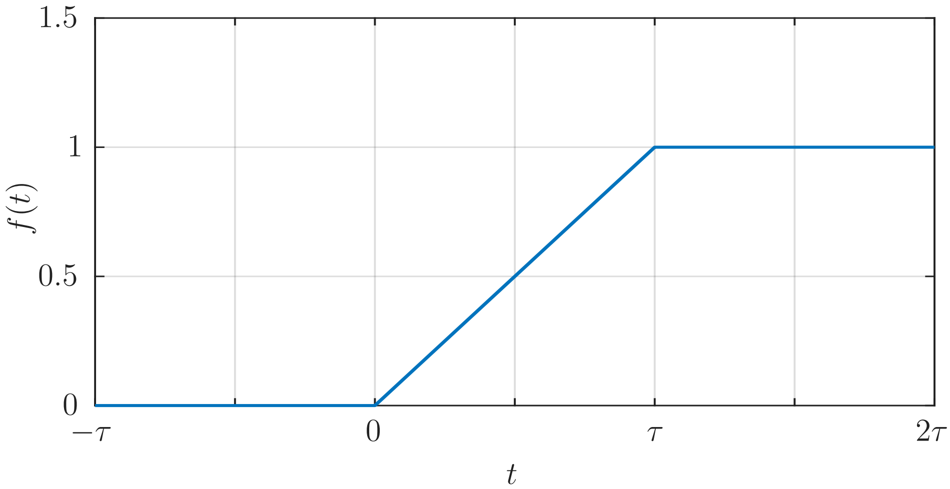

Figure 3.2: Simple loading time-history.

Chapter 4

Method

This work focuses on the analysis of the displacement of a spherically symmetric, viscoelastic, incompressible, self-gravitating, and non rotating planet (from now on, SVISG) under the effect of surface loads. The computation was entrusted to ALMA^3, an open-source program aimed at the calculation of tidal and loading Love numbers. The geometry of the load and the surface displacement were managed by another open-source program, developed specifically to conduct this study, SKAL. Its code is based on another Love numbers and displacement calculator, TABOO.

Three different rheological profiles have been considered and confronted over four time-histories, to evidence the impact of transient rhologies at different timescales.

4.1 Generation of the Love numbers with ALMA^3

ALMA^3 (the plAnetary Love nuMbers cAlculator)[1] is an open source Fortran program aimed at calculating time- and frequency-dependent Love numbers. I will not focus on the implementation and mathematical details of the program; however, it is worth spending a few words regarding its capabilities.

ALMA^3 is able to compute the convoluted Love numbers (see Eq. (3.31)) at given times for a SVISG Earth. It can do so for two different time-histories: instant loading (Eq. (3.34)) and simple loading (Eq. (3.34)). However, since it uses a unit load (see Eq. (3.14)), the calculated LNs can only be used to model AX loads.

Concerning the objectives of this work, ALMA^3's most important characteristic is its capability to manage different rheologies. In particular, it supports all the models described in chapter 2.

However, ALMA^3 does not compute the displacement of the planet, which is the object of study of this work [Melini et al. 2022]. This can be easily calculated using Eq. (3.32). To do so, a new program, SKAL, was developed.

[1] ALMA^3 is available from https://github.com/danielemelini/ALMA3/.

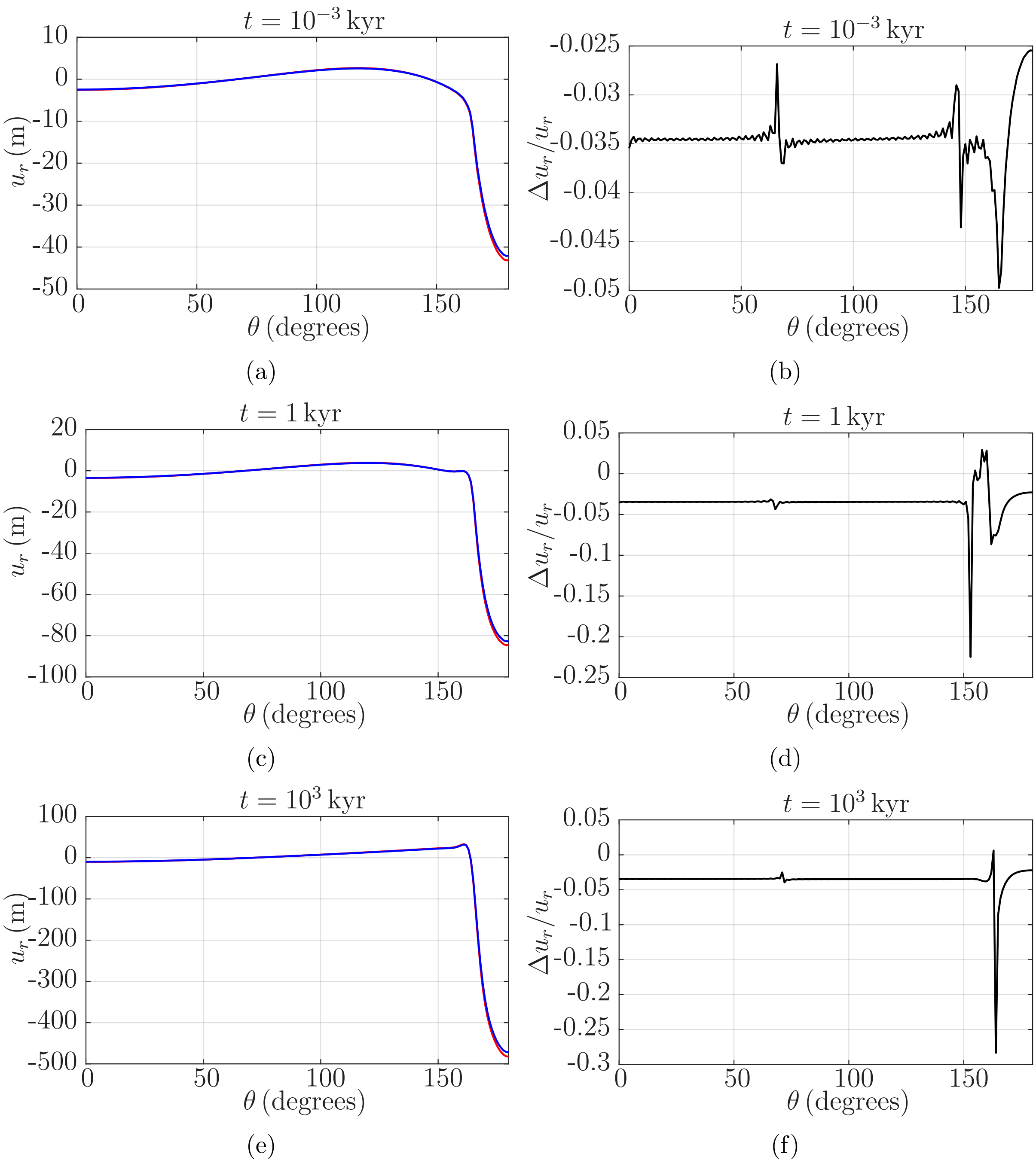

Figure 4.1: In each column, from left to right: radial displacement, radial displacement relative error. TABOO's results are shown in blue, ALMA^3–SKAL's results are shown in red.

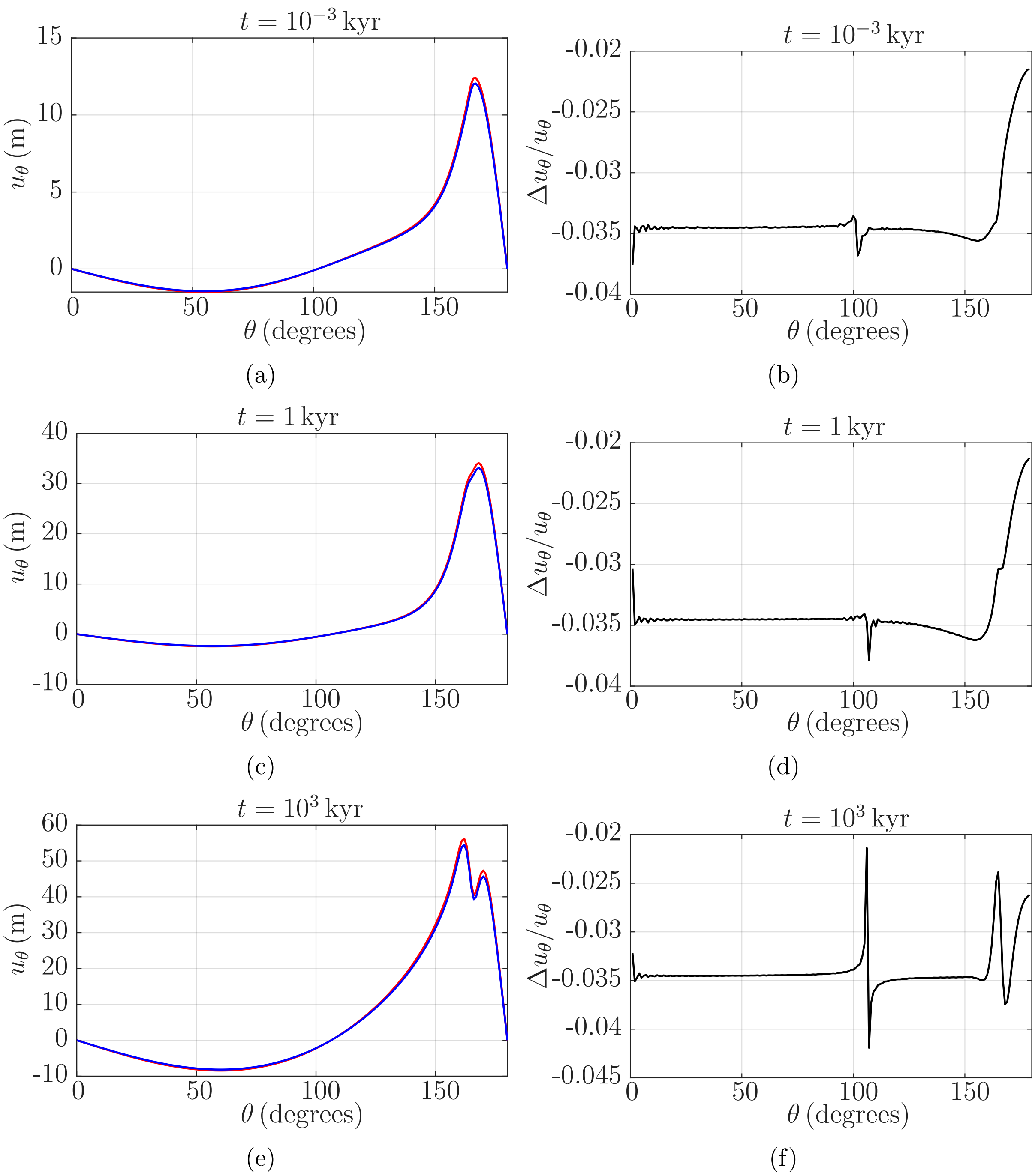

Figure 4.2: In each column, from left to right: latitude displacement, latitude displacement relative error. TABOO's results are shown in blue, ALMA^3–SKAL's results are shown in red.

4.2 Development of SKAL using TABOO

The structure and implementation of SKAL (Simulator of Kinematics from ALMA^3's LLNs)[2] heavily rely on functions already developed for TABOO (a posT-glAcial reBOund calculatOr)[3]. TABOO is able to compute the non-convoluted time-domain Love numbers (which are defined as the inverse Laplace transform of the Laplace-domain Love numbers described in Eq. (3.30)) and the displacement of a SVISG Earth [Spada 2003, 2005].

TABOO offers an ample choice of load functions (including NAX loads) and time-histories, but it is less flexible in terms of rheological properties of the Earth. In particular, it does not support transient rheologies. For this reason, SKAL uses TABOO's spherical harmonic coefficient calculator functions (which implement Eq. (3.6)) and its displacement calculator functions (implementing Eq. (3.32)), and couples them with the ability to read ALMA^3's output files.

The only shared time-history between ALMA^3 and TABOO is instant or step loading; for this reason, it was an obliged choice during the testing phase. The testing was carried out using the reference model of the Earth shown in Table 4.1, using a Maxwell rheology to describe the upper mantle. The load function describes a balanced parabolic load (see Eq. (3.23)) with a thickness of 2 km and an angular radius of 15°, centred over the South Pole.

The response of the Earth to the described load was computed on seven different timescales, from 10^{-3} kyr to 10^3 kyr, using both TABOO and the ALMA^3–SKAL system. The comparison of the results and the relative differences $(u_{TABOO} - u_{A-S})/u_{TABOO}$ along a meridian are reported for three of these timescales in Figures 4.1 and 4.2. Only the radial and latitude components are shown, since the longitude component is correctly computed as null by both programs, due to the axial symmetry of the Earth–load system.

Concerning the relative difference, it exhibits a constant behaviour over time, with an average of -3.5% for both radial and latitude displacement, with spikes where the displacement takes values close to zero. This discrepancy is explained by the different approaches taken by TABOO and ALMA^3 to compute and then convolute the LLNs and the different floating point approximations. Just as an example, ALMA^3 approximates ρ and E, leading to different Earth masses for the two programs: $m_\oplus = 5.970 \cdot 10^{24}$ kg for TABOO and $m_\oplus = 5.943 \cdot 10^{24}$ kg for ALMA^3.

Additional information about the implementation of SKAL is given in appendix B.

4.3 Model

Earth model The Earth model used for this study is based on the averaged values of the PREM [Dziewonski and Anderson 1981], which are shown in Table 4.1. The

[2]SKAL is available from https://github.com/Ciccio-Fonsy/SKAL/.

[3]TABOO is available from https://github.com/danielemelini/TABOO/.

lithosphere is assumed to be 100km thick and the mantle is made of a Burgers upper mantle with steady-state viscosity 10^{21} Pa and a Maxwell lower mantle with viscosity 10^{22} Pa [Cathles 1975].

Layer	Rheology	r (km)	ρ (kg/m^3)	E (GPa)	η (10^{21}Pa $\cdot$ s)
Litho.	Elastic	6371	3193	59.63	–
UM	Maxwell/Burgers	6271	3988	86.99	1.0
LM	Maxwell	5601	4397	219.5	10
Core	Inviscid	3480	10930	–	–

Table 4.1: Rheological parameters for a horizontally homogeneous Earth with a lithosphere thickness of 100 km and a two-layered mantle. Litho. stands for lithosphere, UM for upper mantle, and LM for lower mantle. The transient viscosity of the Burgers layer is not reported, since different configurations have been used. The transient shear modulus is the same as the steady-state shear modulus.

Since ALMA^3 allows full freedom to choose the rheological parameters, this work will focus on the effects of different transient viscosities (labelled η_1 in Figure 2.3 and Eq. (2.24)) of the upper mantle. The transient shear modulus E_1 is equal to the steady-state shear modulus E_2. In particular, three different upper mantle rheologies have been considered: Maxwell rheology (model 0), low-viscosity Burgers rheology with $\eta_1/\eta_2 = 0.1$ (model 1), and high-viscosity Burgers rheology with $\eta_1/\eta_2 = 1$ (model 2). No other values of η_1 have been used, since literature agrees in considering this as the most likely interval for the transient viscosity [Pollitz 2003].

Load geometry The ice takes the shape of a balanced parabolic load (see section 3.1.2) with a maximum thickness of 2 km and an angular radius of 15°, centred over the south pole. The static mass of such a load is $m_s = 1.079 \cdot 10^{19}$ kg, with ice density $\rho_i = 931$ kg/m^3.

Time-history For the first set of experiments, a Heaviside loading, described in Eq. (3.34), has been used. Otherwise, the chosen time-history is a ramp loading, described in Eq. (3.36) and shown in Figure 3.2, with the duration of the loading process, τ, varying from 1 kyr to 100 kyr.

Local study Since the system is axisymmetric and the axis of symmetry corresponds to the Earth's rotation axis, there is no expected variation of the displacement along a parallel. For this reason, the displacement is computed along the Greenwich meridian (this is done only for convenience, since the longitude of the meridian does not influence the outcome), and only the radial and latitude components will be shown, the longitude component being zero.

4.4 Analysis of the displacement

Radial and latitude displacement was computed at different times for three rheologies and four time-histories. For any given time, displacement is shown as a function of colatitude, with a resolution of $1°$. The displacements for different rheologies were then compared with each other. The difference in displacement is also shown as a function of colatitude. A short term and a long term study have been executed: for the short term study, the time step is 50 yr, from 50 yr after the beginning of the loading process to 1000 yr; for the long term study, the displacement and displacement differences are shown at intervals of 1 kyr for times 1 kyr $\leq t \leq$ 20 kyr, while for times up to 100 kyr after the initial loading the interval becomes 5 kyr. To each time corresponds a different shade:

- blue for 50 yr $\leq t \leq$ 200 yr in short term studies and 1 kyr $\leq t \leq$ 5 kyr in the long term,
- teal for 250 yr $\leq t \leq$ 400 yr in the short term and 6 kyr $\leq t \leq$ 10 kyr in the long term,
- lime for 450 yr $\leq t \leq$ 600 yr in the short term and 11 kyr $\leq t \leq$ 15 kyr in the long term,
- yellow for 650 yr $\leq t \leq$ 800 yr in the short term and 16 kyr $\leq t \leq$ 20 kyr in the long term,
- orange for 850 yr $\leq t \leq$ 1000 yr in the short term and 25 kyr $\leq t \leq$ 45 kyr in the long term,
- red for 50 kyr $\leq t \leq$ 70 kyr, this and the following used in long term studies only,
- brown for 75 kyr $\leq t \leq$ 100 kyr.

The evolution of some geophysical benchmarks has also been studied. The first study was conducted at the point of maximum subsidence, its location corresponding to the South pole. The evolution of the forebulge that surrounds the subsided region has also been studied in terms of radial and latitude displacement. It can be easily seen on the radial displacement graph as its absolute maximum and on the latitude displacement graph as its first local maximum, but only after an average time of 3 kyr after the beginning of the loading process. Another benchmark point has been studied on the latitude displacement graph, which is its second local maximum (or the only one, before the peak associated with the forebulge is formed).

Chapter 5

Results

In the following pages, the results of the different experiments are shown. In particular, Figures 5.1 and 5.2 show the short and long term response of the different rheologies to an instant loading (Eq. (3.34), from now on referred to as history 0), Figures 5.3 and 5.4 refer to simple loadings (Eq. (3.36)) with a loading phase duration of 1 kyr (history 1), Figures 5.5 and 5.6 show the response to a simple loading with a duration of 10 kyr (history 10), and Figures 5.7 and 5.8 refer to a loading phase of 100 kyr (history 100). Sub-figures (a) and (b) always refer, respectively, to the radial and latitude displacement of the Maxwell upper mantle rheology (model 0), (c) and (d) refer to the same quantities for the Burgers rheology with viscosities $\eta_1/\eta_2 = 0.1$ (model 1), (e) and (f) concern the Burgers rheology with $\eta_1/\eta_2 = 1$ (model 2).

Next, the difference in displacement for the different rheologies on the same time-history is shown: Figures 5.9 and 5.10 refer to history 0, Figures 5.11 and 5.12 to history 1, Figures 5.13 and 5.14 to history 10, and Figures 5.15 and 5.16 to history 100. In this set of figures, graphs (a) and (b) represent, respectively, $u_r^1 - u_r^0$ and $u_\theta^1 - u_\theta^0$, where the superscript index refers to the rheological model, graphs (c) and (d) show $u_r^2 - u_r^0$ and $u_\theta^2 - u_\theta^0$, and graphs (e) and (f) refer to $u_r^2 - u_r^1$ and $u_\theta^2 - u_\theta^1$.

In the aforementioned figures, short term analysis is performed at intervals of 50 yr from 50 yr to 1000 yr after the beginning of the loading, while long term analysis extends over a span of 99 kyr, from 1 kyr to 100 kyr after the initial loading, with steps of 1 kyr until 20 kyr after the loading and 5 kyr for higher times; the images use the colour codes described in section 4.4.

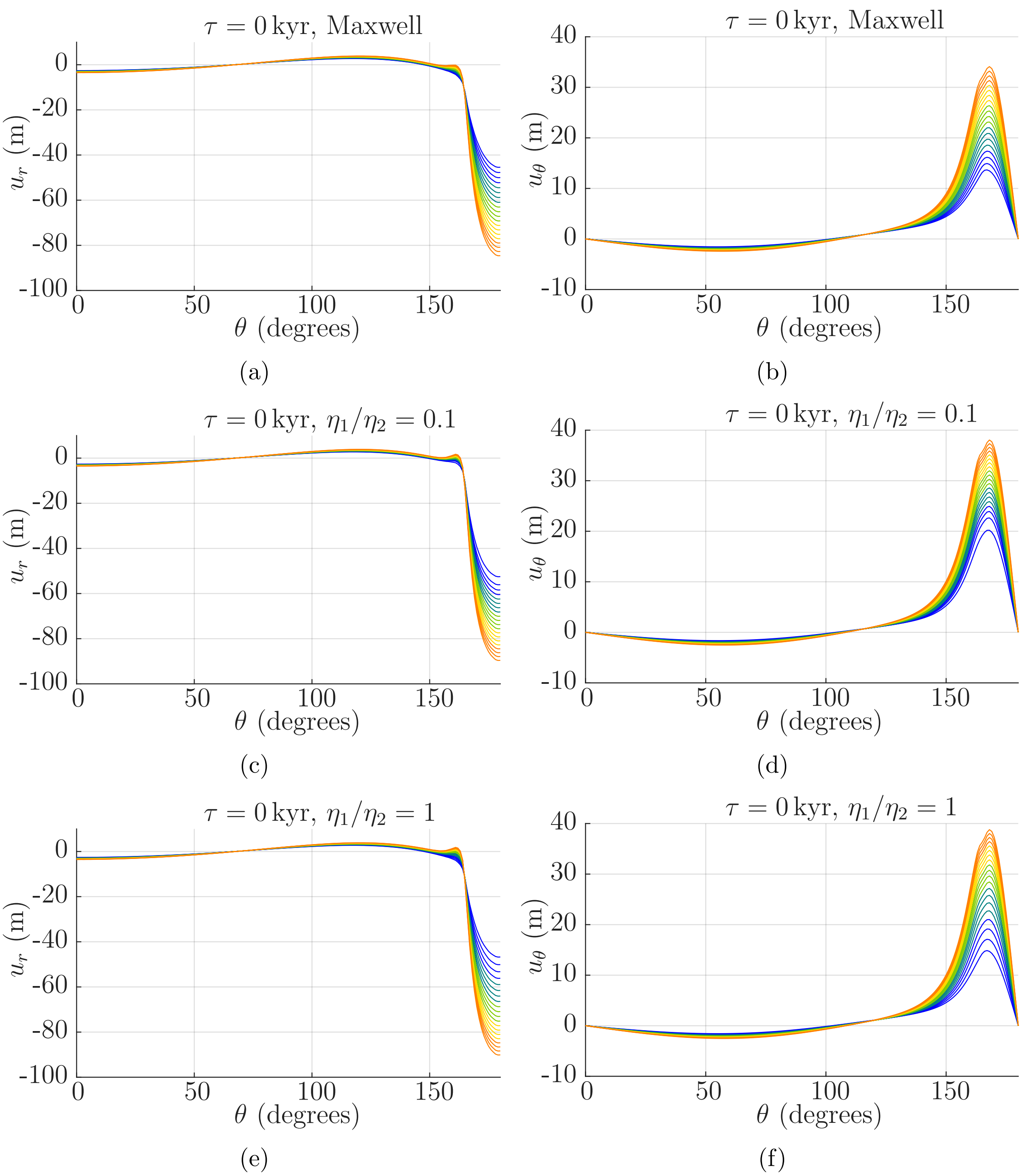

Figure 5.1: Short term analysis of radial and latitude displacement in response to an instant loading for three different rheologies of the upper mantle; from top to bottom: Maxwell, Burgers with $\eta_1/\eta_2 = 0.1$, Burgers with $\eta_1/\eta_2 = 1$.

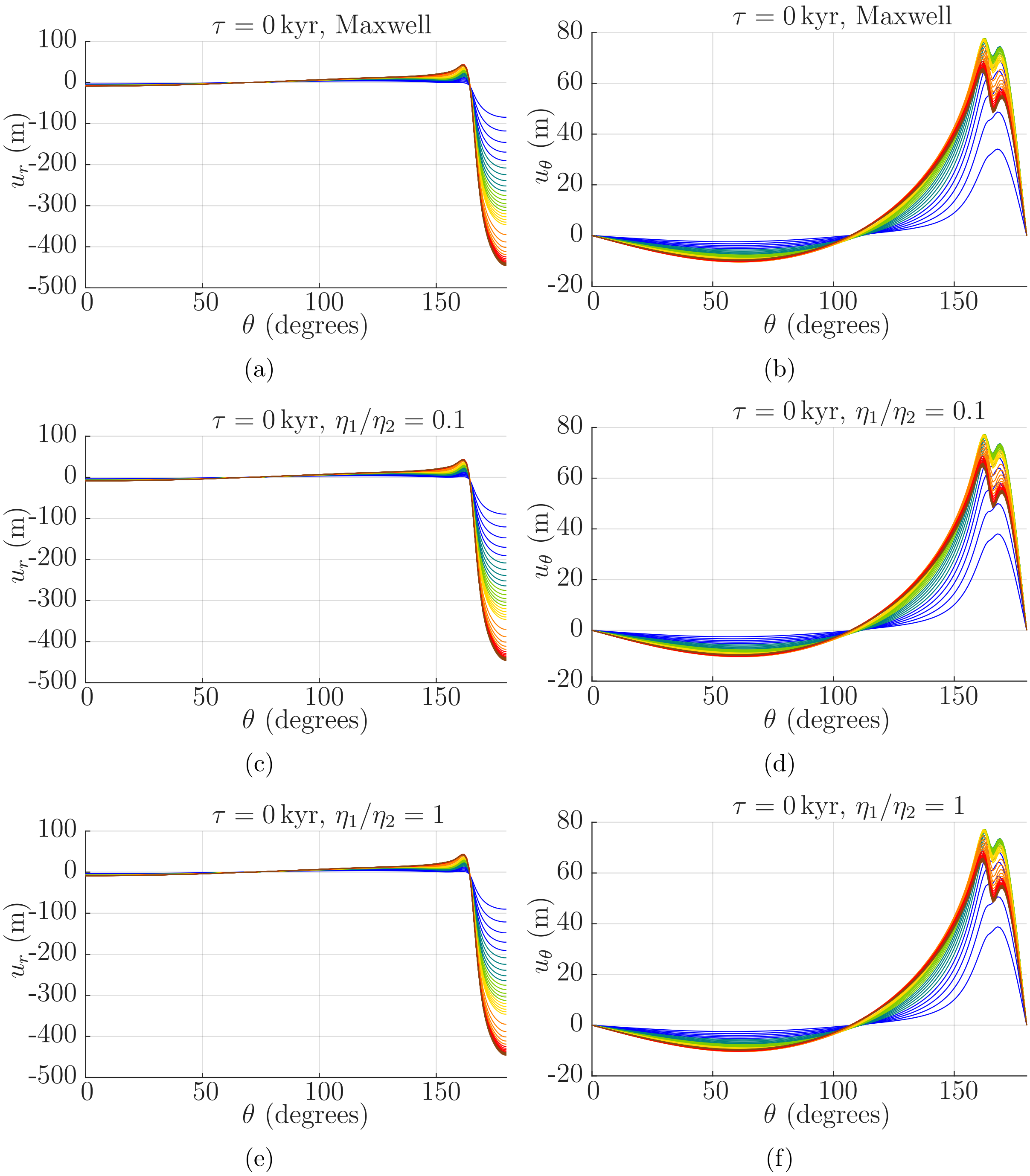

Figure 5.2: Long term analysis of radial and latitude displacement in response to an instant loading for three different rheologies of the upper mantle; from top to bottom: Maxwell, Burgers with $\eta_1/\eta_2 = 0.1$, Burgers with $\eta_1/\eta_2 = 1$.

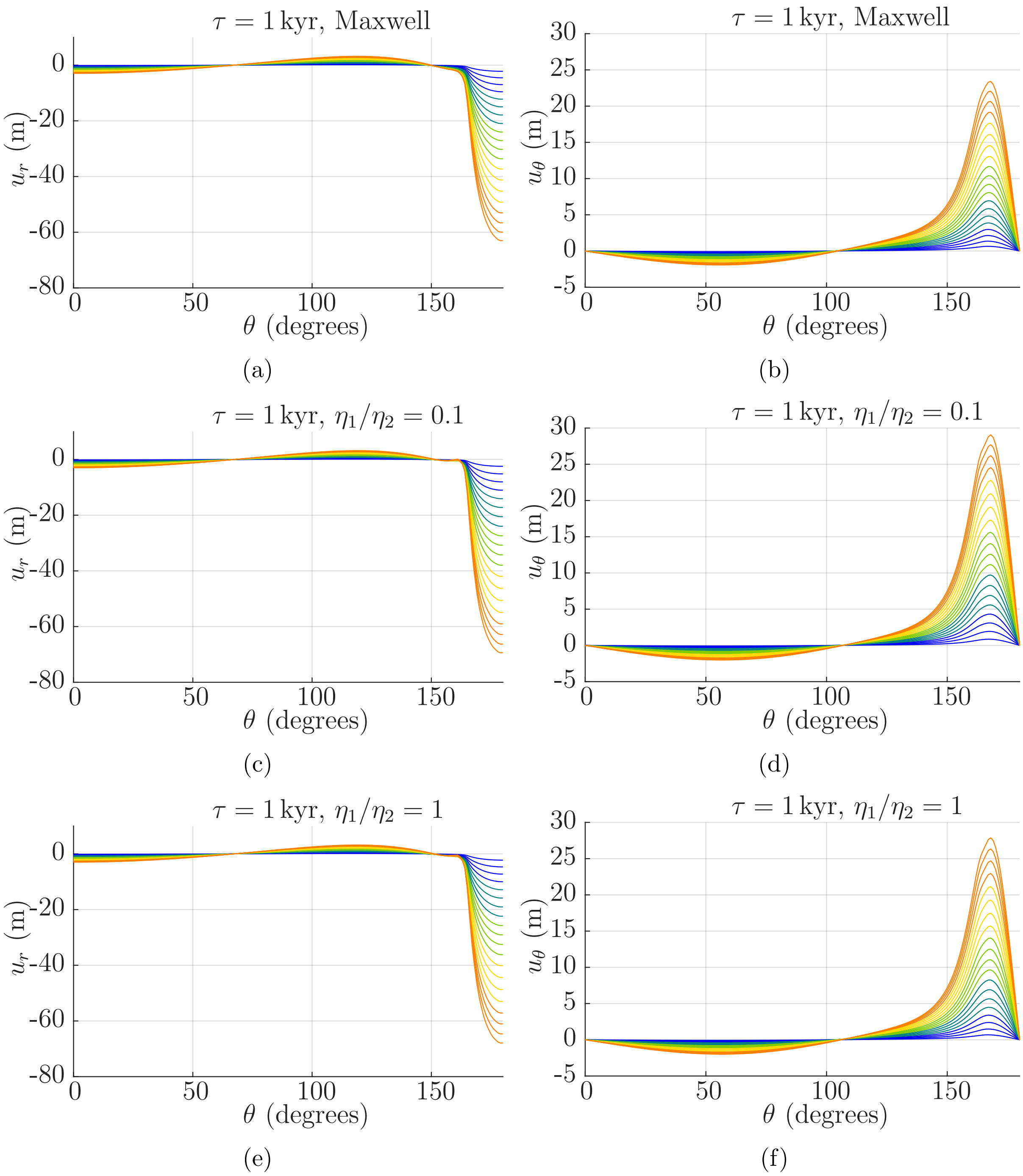

Figure 5.3: Short term analysis of radial and latitude displacement in response to a simple loading with a duration $\tau = 1$ kyr for three different rheologies of the upper mantle; from top to bottom: Maxwell, Burgers with $\eta_1/\eta_2 = 0.1$, Burgers with $\eta_1/\eta_2 = 1$.

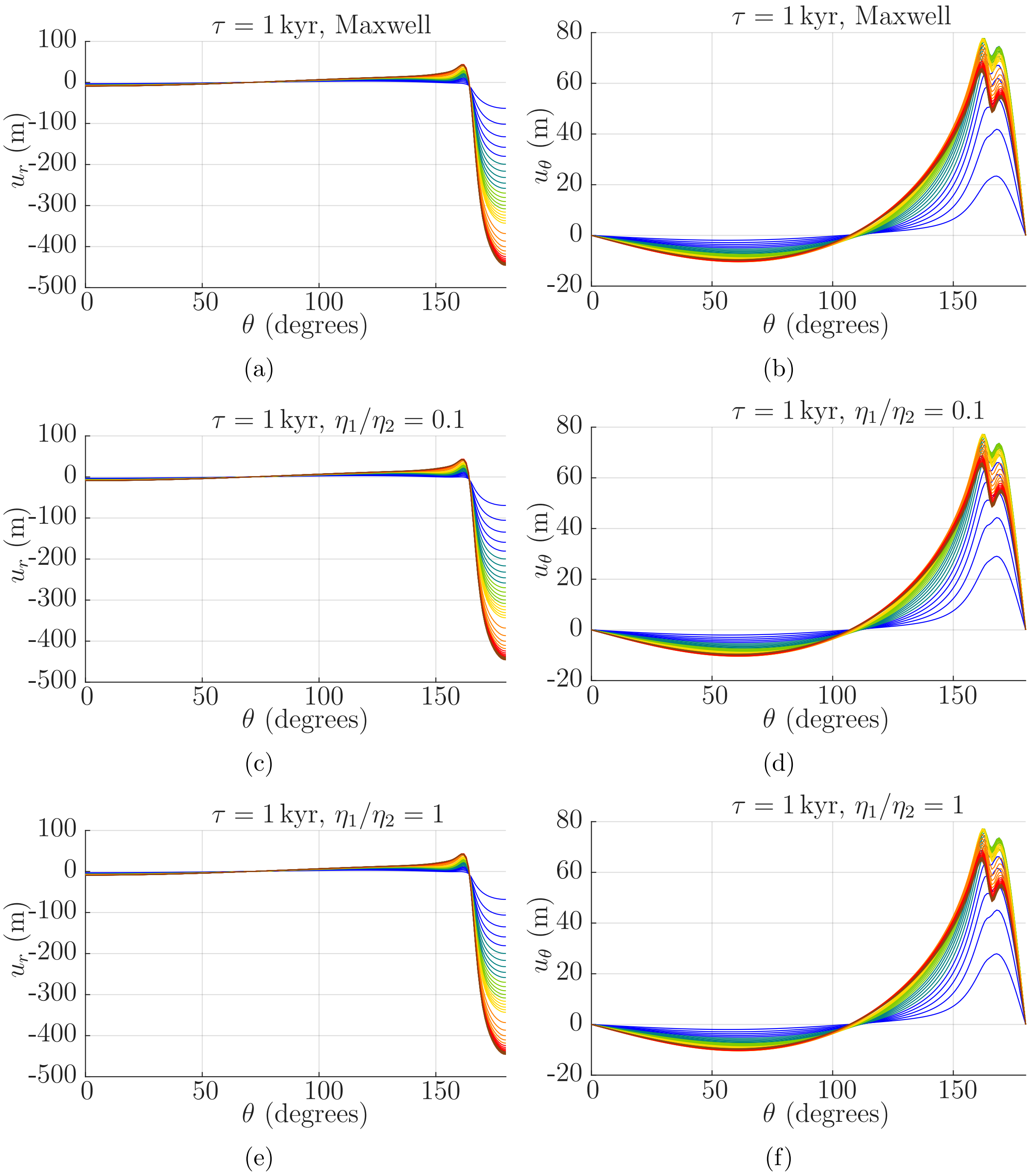

Figure 5.4: Long term analysis of radial and latitude displacement in response to a simple loading with a duration $\tau = 1$ kyr for three different rheologies of the upper mantle; from top to bottom: Maxwell, Burgers with $\eta_1/\eta_2 = 0.1$, Burgers with $\eta_1/\eta_2 = 1$.

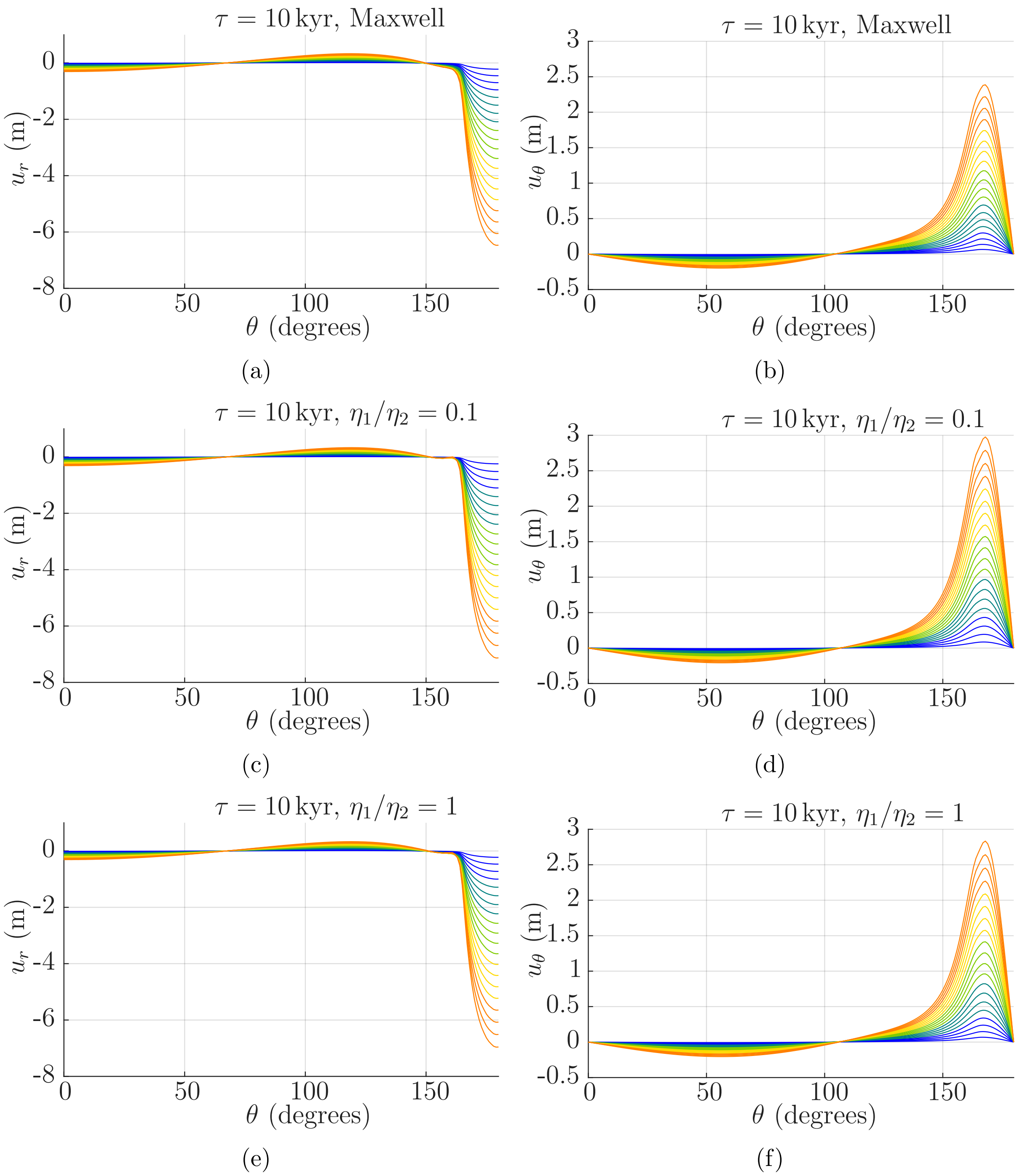

Figure 5.5: Short term analysis of radial and latitude displacement in response to a simple loading with a duration $\tau = 10$ kyr for three different rheologies of the upper mantle; from top to bottom: Maxwell, Burgers with $\eta_1/\eta_2 = 0.1$, Burgers with $\eta_1/\eta_2 = 1$.

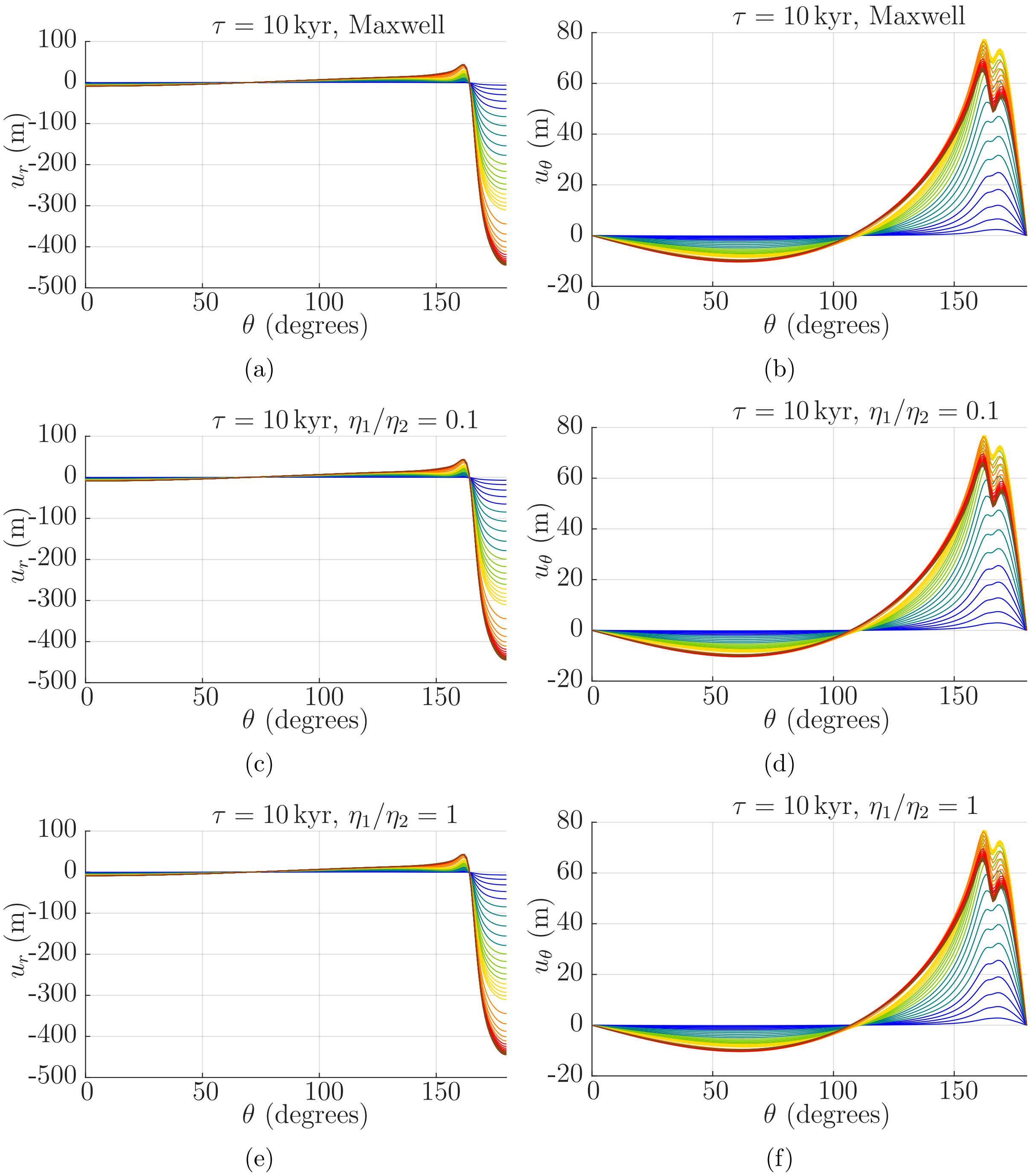

Figure 5.6: Long term analysis of radial and latitude displacement in response to a simple loading with a duration $\tau = 10$ kyr for three different rheologies of the upper mantle; from top to bottom: Maxwell, Burgers with $\eta_1/\eta_2 = 0.1$, Burgers with $\eta_1/\eta_2 = 1$.

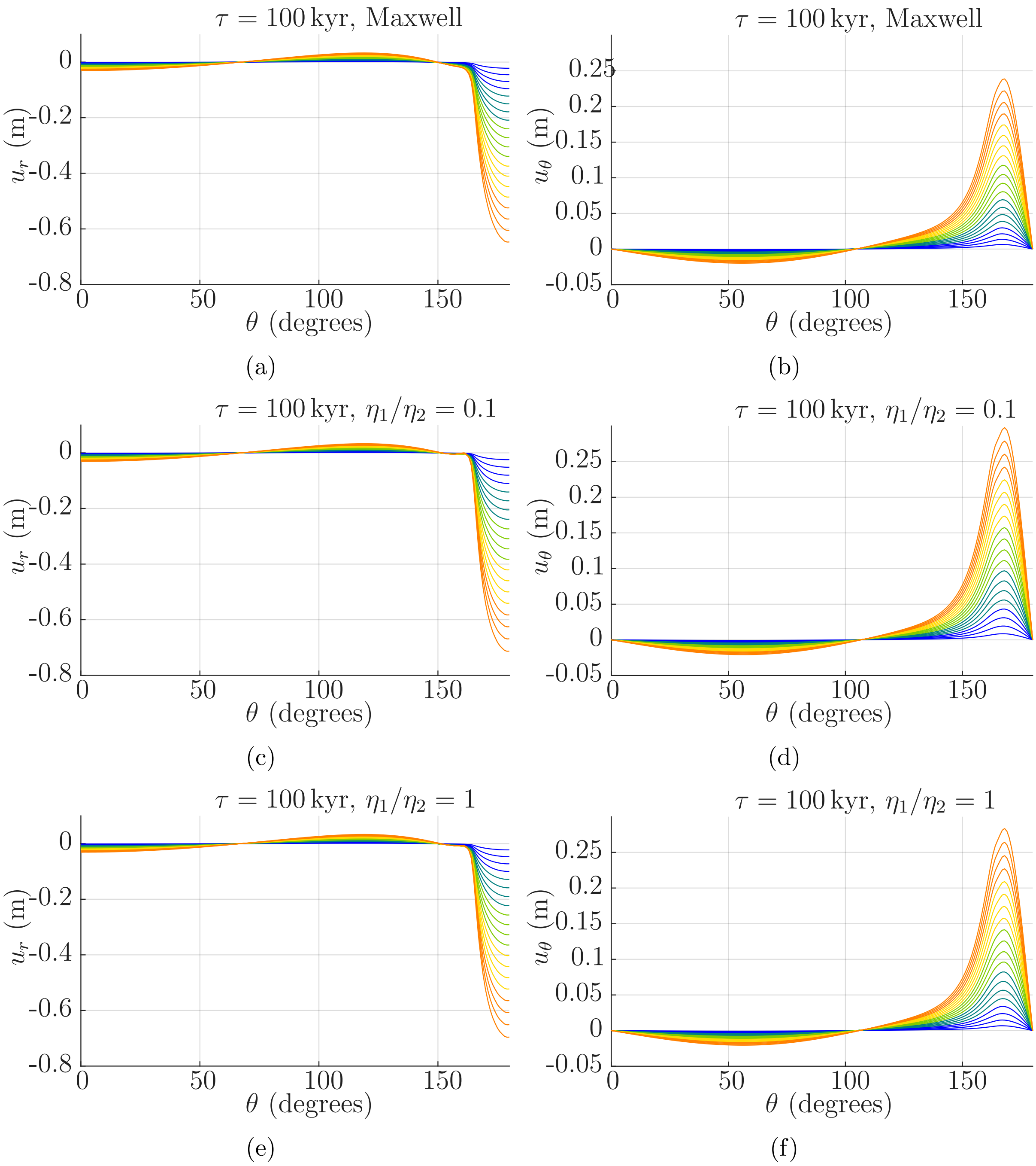

Figure 5.7: Short term analysis of radial and latitude displacement in response to a simple loading with a duration $\tau = 100$ kyr for three different rheologies of the upper mantle; from top to bottom: Maxwell, Burgers with $\eta_1/\eta_2 = 0.1$, Burgers with $\eta_1/\eta_2 = 1$.

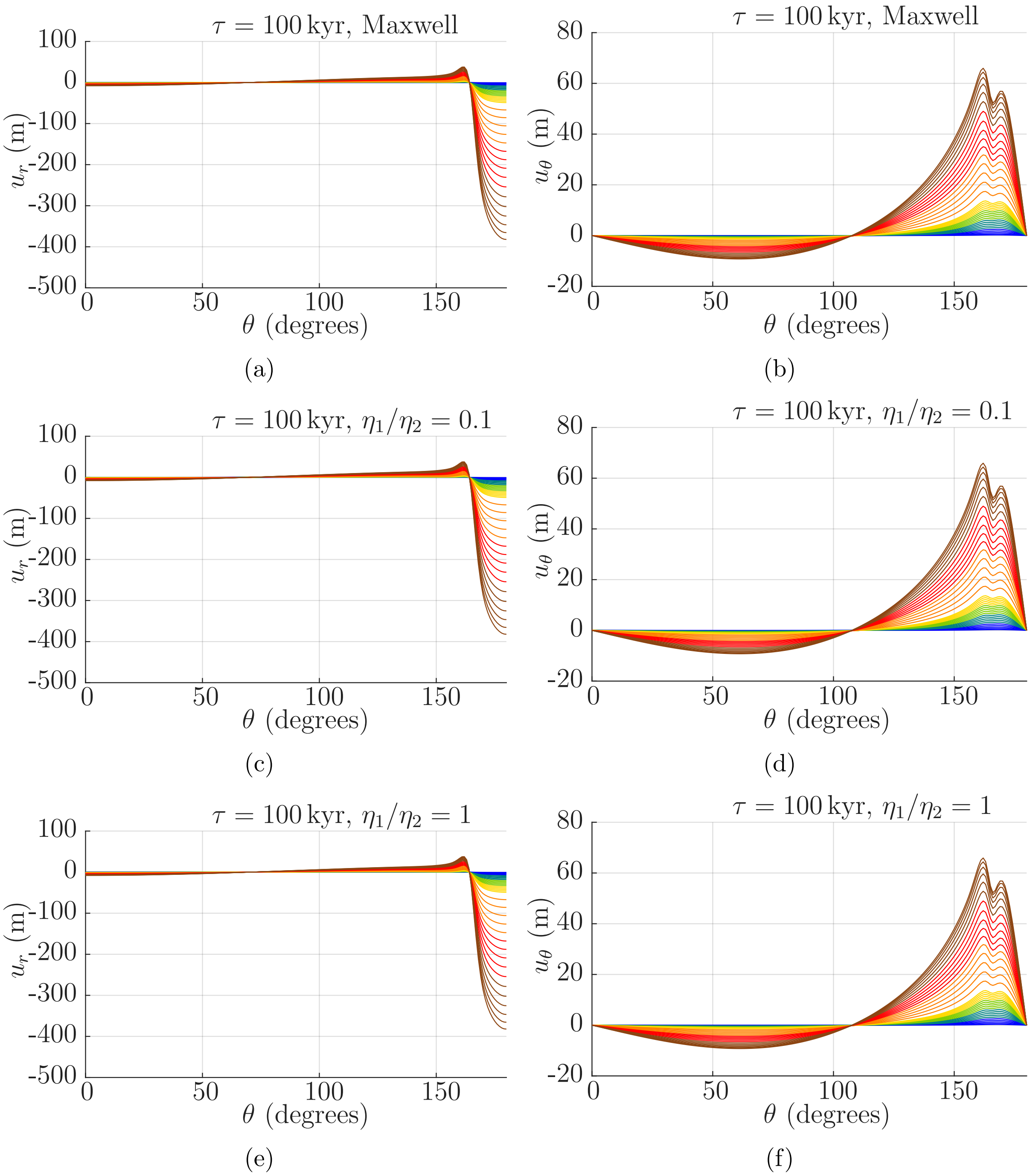

Figure 5.8: Long term analysis of radial and latitude displacement in response to a simple loading with a duration $\tau = 100$ kyr for three different rheologies of the upper mantle; from top to bottom: Maxwell, Burgers with $\eta_1/\eta_2 = 0.1$, Burgers with $\eta_1/\eta_2 = 1$.

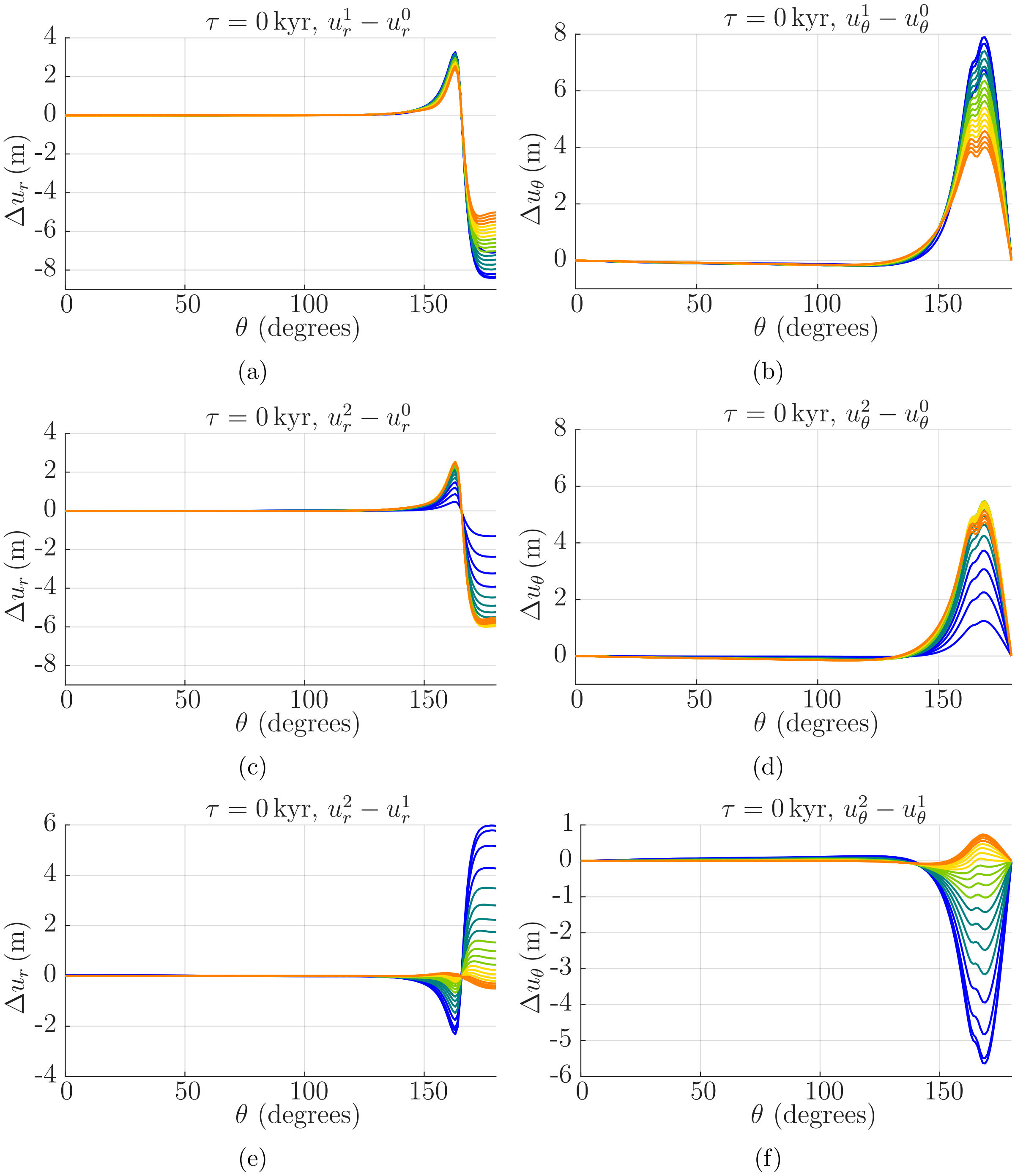

Figure 5.9: Short term analysis of difference in displacement to an instant loading for different rheologies; from top to bottom: low viscosity Burgers and Maxwell, high viscosity Burgers and Maxwell, high viscosity and low viscosity Burgers.

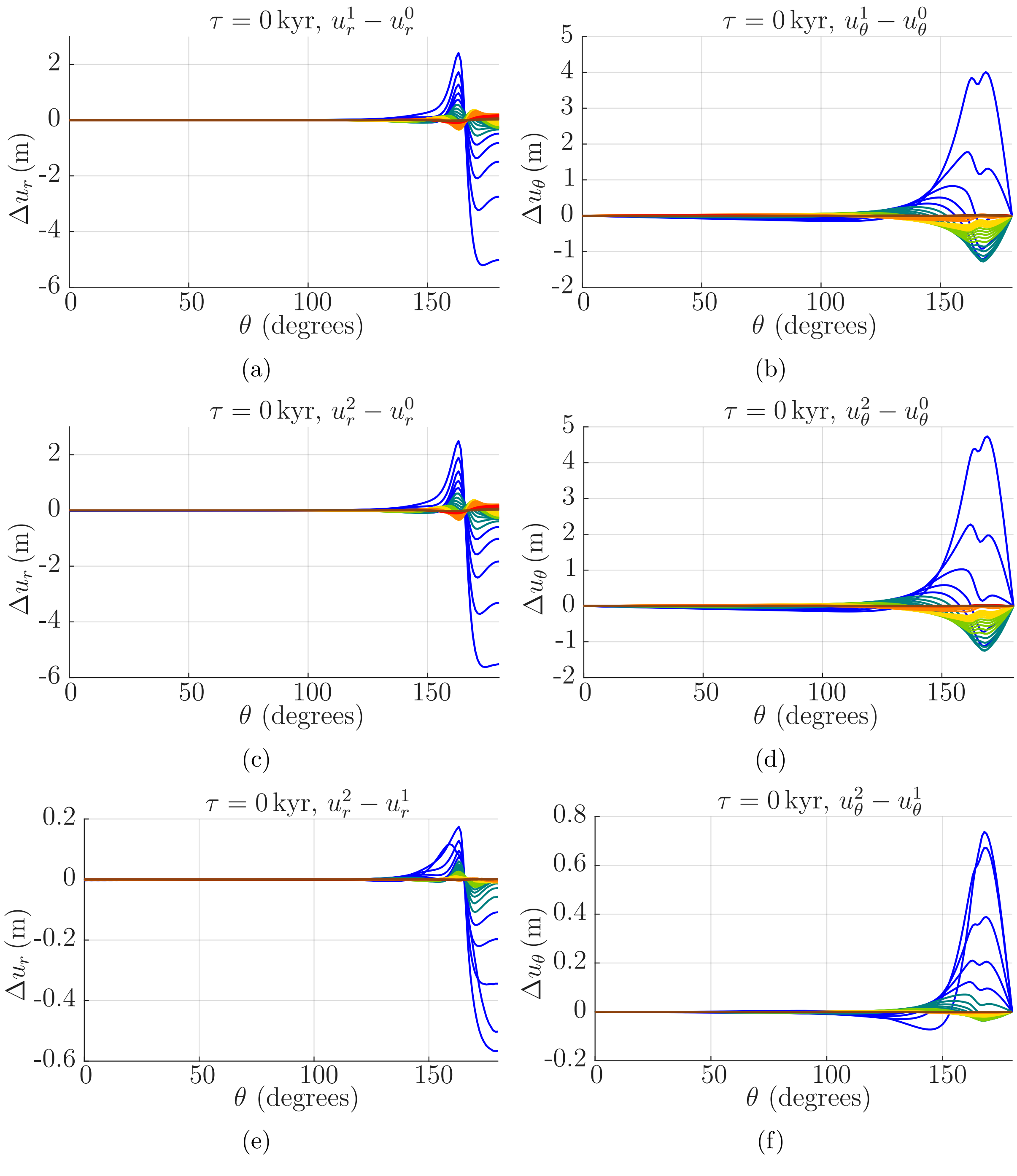

Figure 5.10: Long term analysis of difference in displacement to an instant loading for different rheologies; from top to bottom: low viscosity Burgers and Maxwell, high viscosity Burgers and Maxwell, high viscosity and low viscosity Burgers.

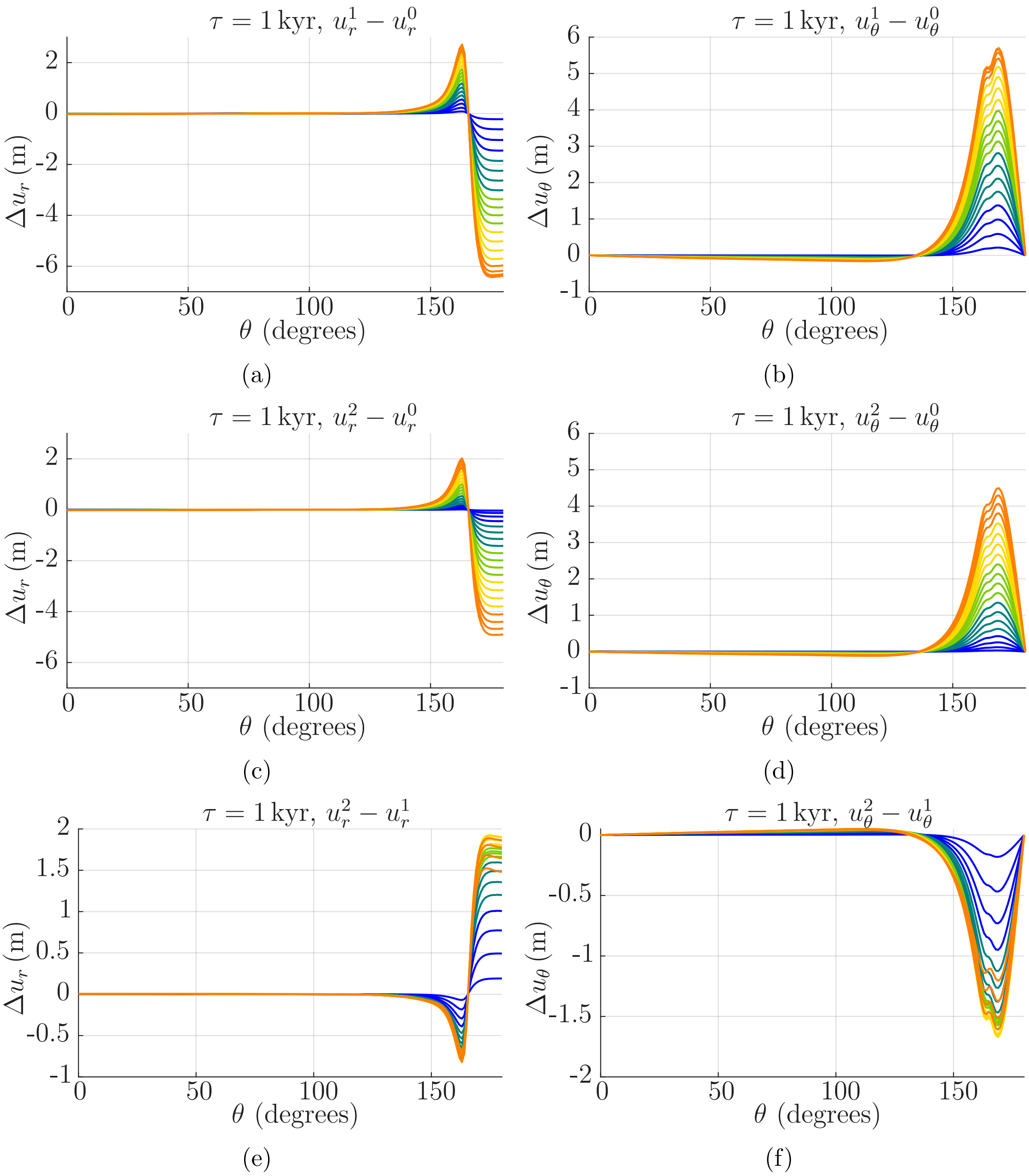

Figure 5.11: Short term analysis of difference in displacement to a simple loading with a duration $\tau = 1$ kyr for different rheologies; from top to bottom: low viscosity Burgers and Maxwell, high viscosity Burgers and Maxwell, high viscosity and low viscosity Burgers.

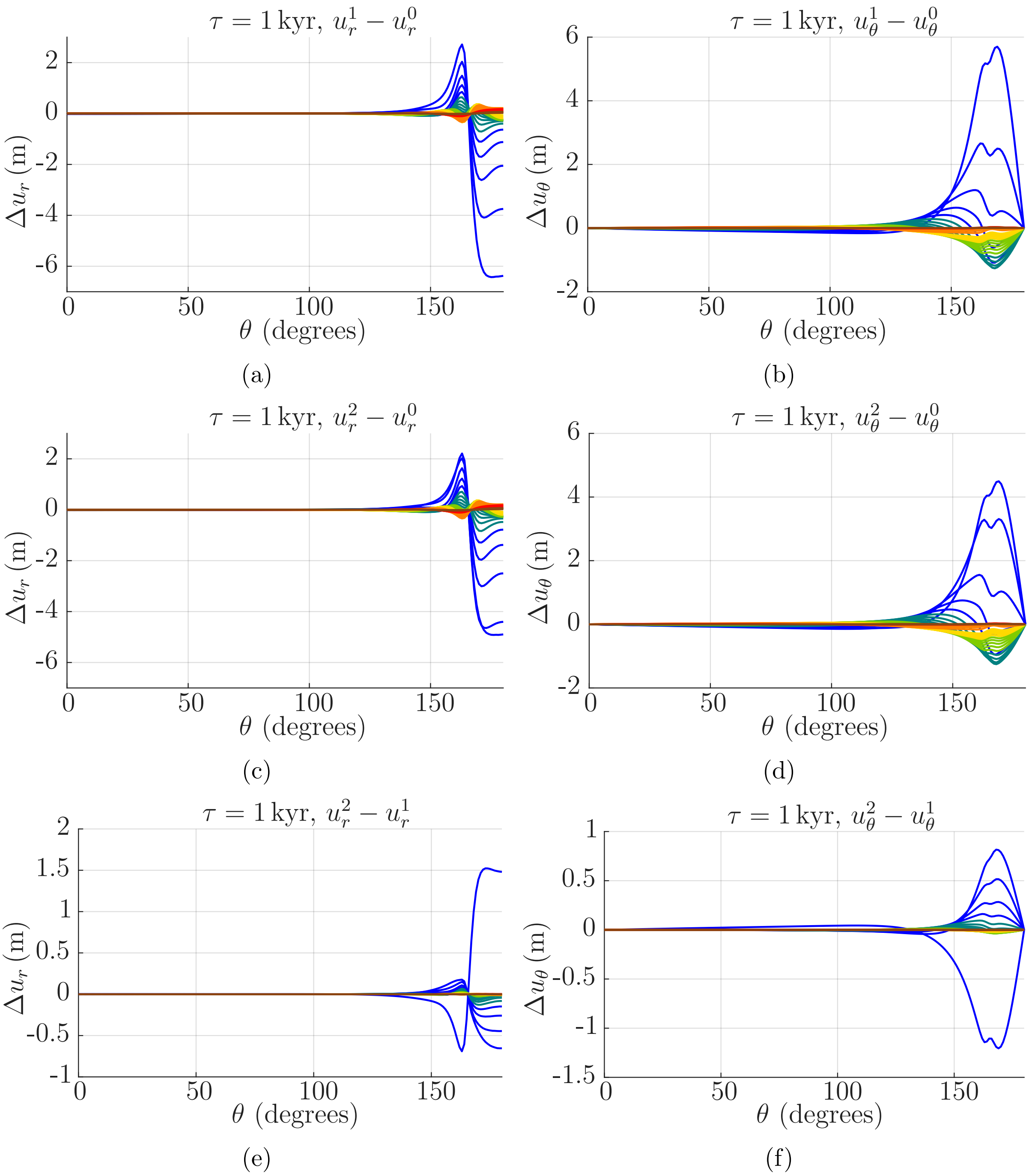

Figure 5.12: Long term analysis of difference in displacement to a simple loading with a duration $\tau = 1$ kyr for different rheologies; from top to bottom: low viscosity Burgers and Maxwell, high viscosity Burgers and Maxwell, high viscosity and low viscosity Burgers.

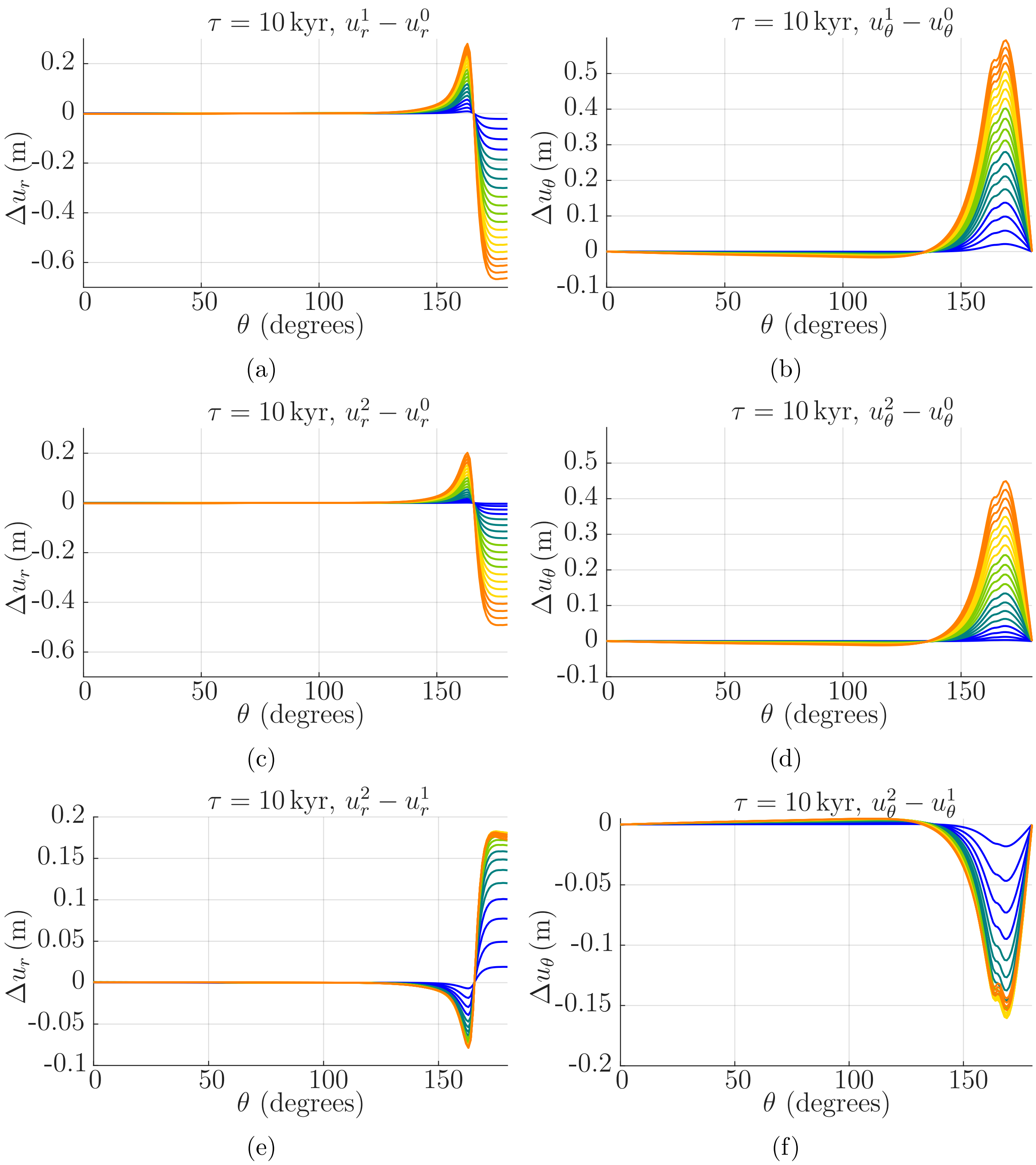

Figure 5.13: Short term analysis of difference in displacement to a simple loading with a duration $\tau = 10$ kyr for different rheologies; from top to bottom: low viscosity Burgers and Maxwell, high viscosity Burgers and Maxwell, high viscosity and low viscosity Burgers.

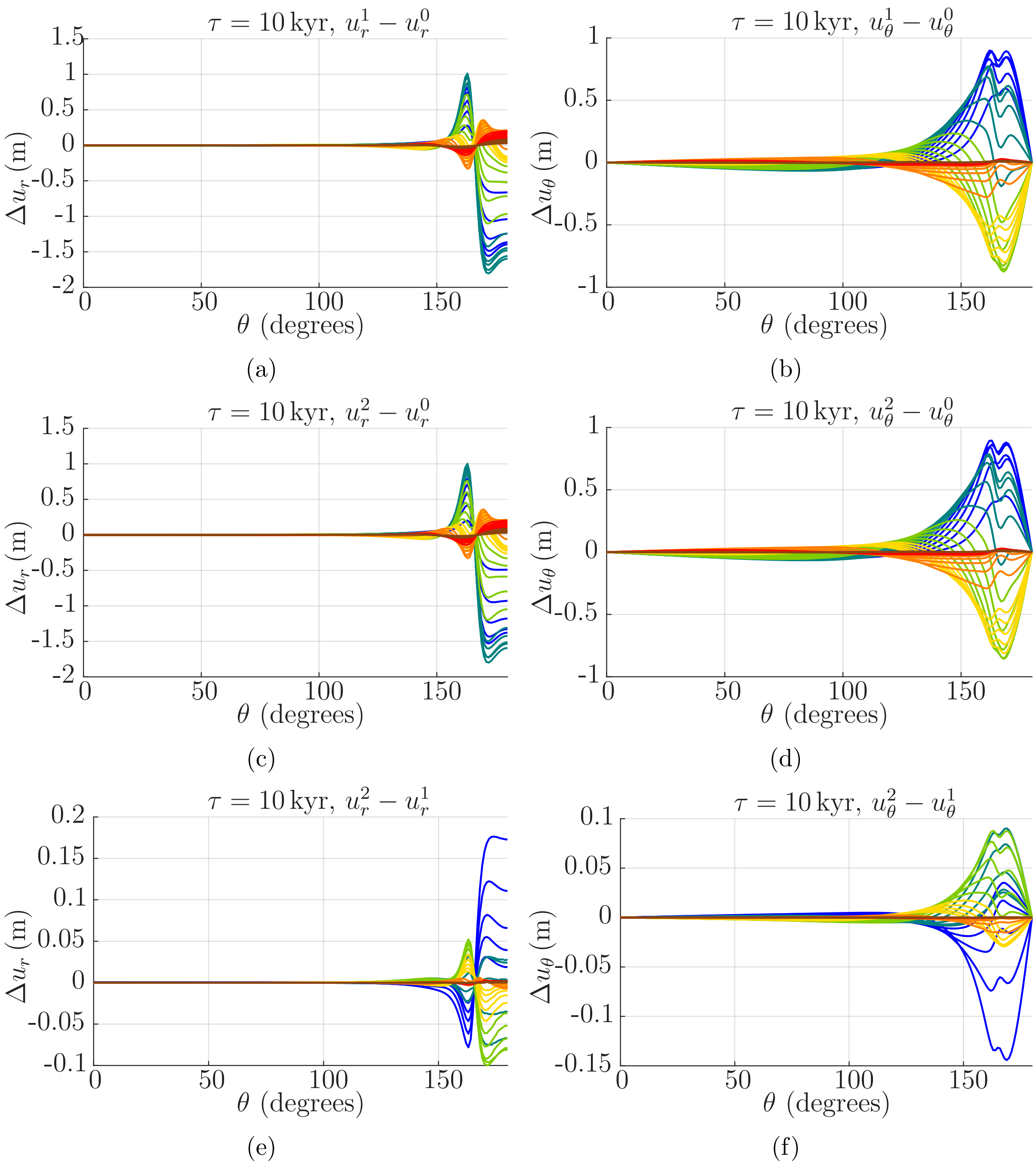

Figure 5.14: Long term analysis of difference in displacement to a simple loading with a duration $\tau = 10$ kyr for different rheologies; from top to bottom: low viscosity Burgers and Maxwell, high viscosity Burgers and Maxwell, high viscosity and low viscosity Burgers.

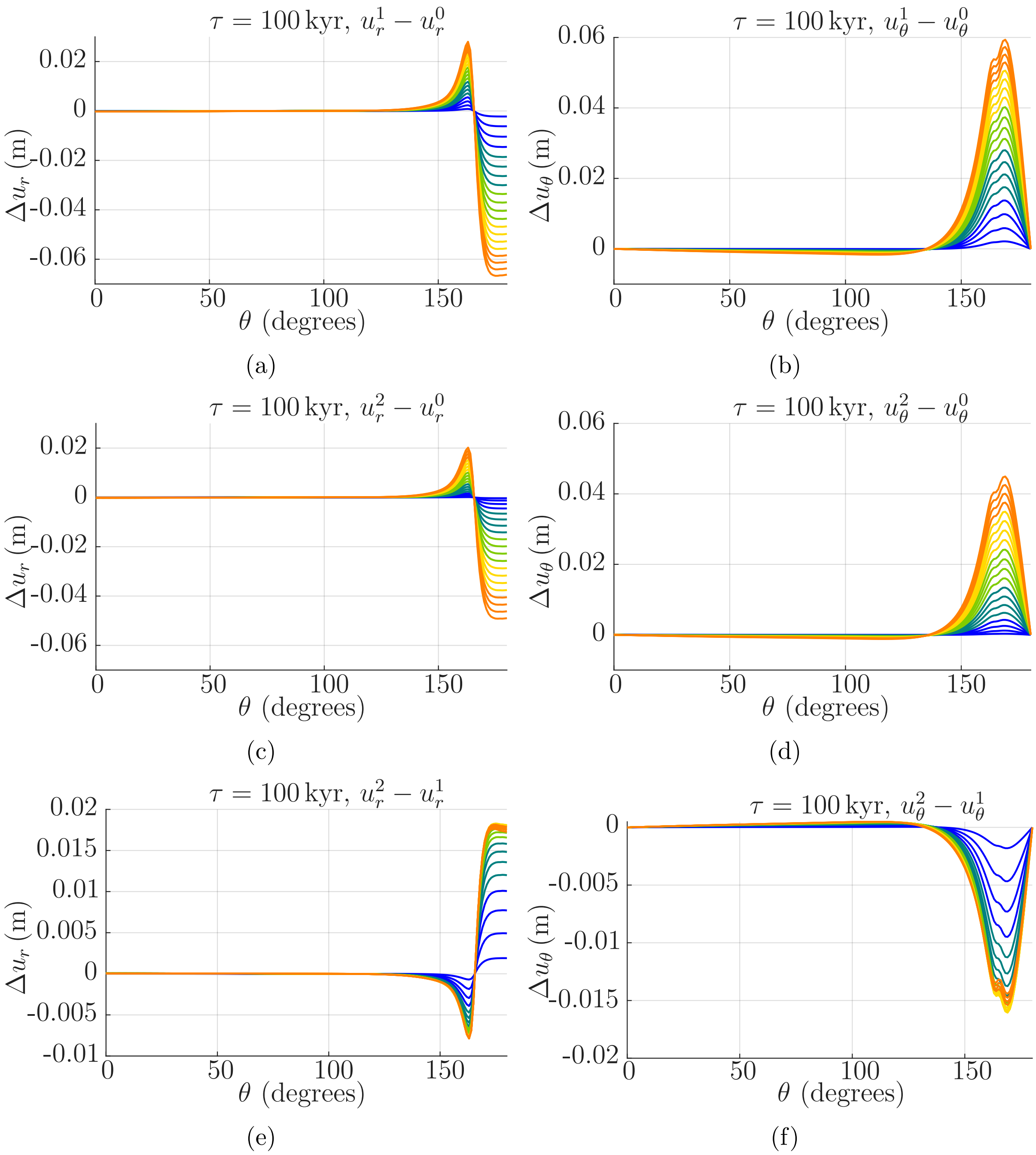

Figure 5.15: Short term analysis of difference in displacement to a simple loading with a duration $\tau = 100$ kyr for different rheologies; from top to bottom: low viscosity Burgers and Maxwell, high viscosity Burgers and Maxwell, high viscosity and low viscosity Burgers.

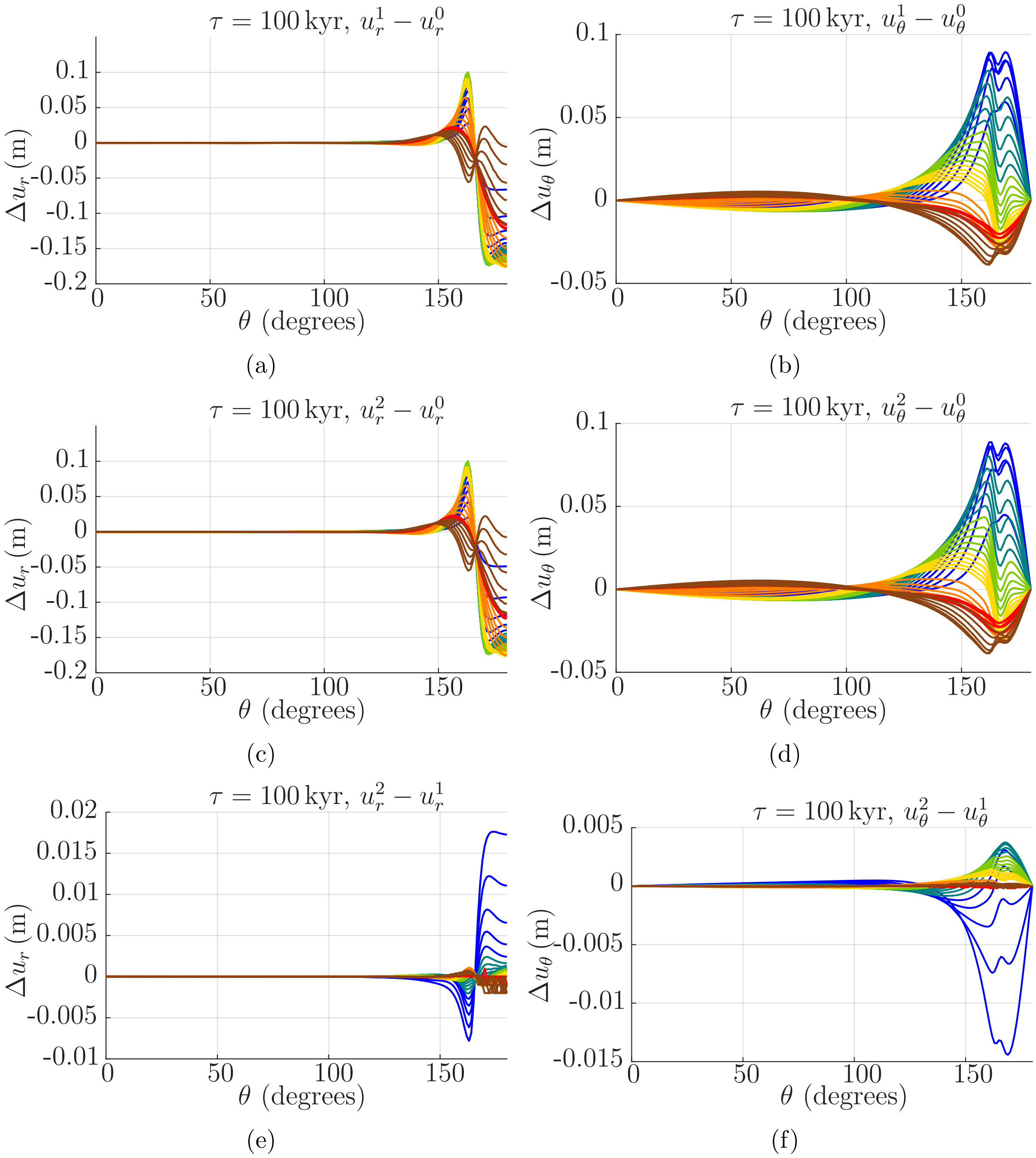

Figure 5.16: Long term analysis of difference in displacement to a simple loading with a duration $\tau = 100$ kyr for different rheologies; from top to bottom: low viscosity Burgers and Maxwell, high viscosity Burgers and Maxwell, high viscosity and low viscosity Burgers.

5.1 Analysis

To comprehend the effects of the usage of Burgers rheology, it is important to determine the characteristic times of the different rheological profiles: relaxation and retardation times. For a Maxwell rheology (described in Section 2.3), only the relaxation time $\tau = \eta/E$ is defined. For a Burgers rheology (described in Section 2.5), the retardation time is defined as $\tau_{ret} = \eta_1/E_1$, while two relaxation times exist: $\tau_1 = \eta_1'/E_1'$ and $\tau_2 = \eta_2'/E_2'$; η_1 and E_1 are the transient viscosity and shear modulus in the Maxwell-Kelvin description of the material (as shown in Figure 2.3), while η_1', η_2', E_1' and E_2' are the viscosities and shear moduli of the two branches in the generalized Maxwell description (as shown in Figure 2.4). Since the rheological parameters are initially defined in the Maxwell-Kelvin representation, Eq. (2.28) must be used to obtain the parameters in the generalized Maxwell representation and the relaxation times. The values of the characteristic times are shown in Table 5.1.

τ^{LM}	τ^0	τ_1^1	τ_2^1	τ_{ret}^1	τ_1^2	τ_2^2	τ_{ret}^2
1444	364.3	747.2	17.76	36.43	953.7	139.1	364.3

Table 5.1: Characteristic times of the different rheological models in years. τ^{LM} is the relaxation time of the lower mantle, while the other superscript indexes refer to the specific rheological model of the upper mantle.

The time histories can be roughly divided into three groups: history 0, which showcases peculiar characteristics due to the instant loading, history 1, where the duration of the process is comparable to the timescales of the rheological models, and histories 10 and 100, with processes much longer than the characteristic times.

The initial behaviour is similar for each of the experiments: the radial displacement differences between a Burgers and a Maxwell upper mantle rheology show a similar qualitative trend for both the transient models. The difference initially grows, the duration of this phase increasing with the transient viscosity and the duration of the loading process. The maximum value of the difference, on the other hand, decreases as the viscosity and the duration of the loading increase. This is consistent with the fact that a Maxwell fluid can be seen as a Burgers body with infinite transient viscosity.

For long term loadings (like histories 10 and 100) the maximum difference is inversely proportional to the duration of the process, while the duration of the difference increase is linearly dependent from the duration of the loading phase, as can be seen by comparing Figures 5.14a and 5.16a, and Figures 5.14c and 5.16c.

The magnitude of the latitude difference is also inversely related to the duration of the loading process, but it reaches its peak at about 3 kyr after the initial loading for both history 10 and history 100, as can be seen from the comparison of Figures 5.14b and 5.16b, and Figures 5.14d and 5.16d.

In the short term, the difference between model 1 and model 2 is about one third of those between Burgers and Maxwell models, as can be seen by comparing Figure 5.11e with 5.11a and 5.11c, 5.13e with 5.13a and 5.13c, and 5.11e with 5.15a and 5.15c for the radial displacement, and Figure 5.11f with 5.11b and 5.11d, 5.13f with 5.13b and 5.13d, and 5.15f with 5.15b and 5.15d for the latitude displacement.

In case of simple loading, the maximum difference between model 1 and model 2 is always observed 750 yr after the beginning of the loading for both radial and latitude displacement, independently from the duration of the loading. This can be seen by looking at Figures 5.11e, 5.11f, 5.13e, 5.13f, 5.15e and 5.15f. The value of the maximum value is inversely proportional to the duration of the loading, and thus directly proportional to its rate of change.

Under the effect of instant loading, which can be used as a limit case to model extremely fast loading processes, the behaviour of the Earth is different. The maximum difference between model 1 and model 0 is reached 100 yr after the loading, while the maximum difference between model 2 and model 0 is reached after 650 yr. It is safe to assume that the maximum value assumed with this time-history is the highest possible, since it decreases with the duration of the loading. This could be said for the difference between model 2 and model 1 too. However, the two transient models have already reached their maximum difference 50 yr after the loading.

On the long term, the Earth-load system reaches an equilibrium that does not depend on the transient properties or the specific time-history. The maximum depth of the subsided region increases asymptotically to 480 m, while the forebulge reaches a maximum height of about 43 m, then it starts to slowly decrease.

5.1.1 Subsided region

It can be immediately seen that, at the maximum depth of the subsided region, the relative displacement difference is extremely significant in the short term, where $\Delta u_r/u_r \approx 10\%$ and $\Delta u_\theta/u_\theta \approx 20\%$, as can be seen, for example, comparing Figure 5.7 to Figure 5.15.

The value of the maximum relative difference, as well as the time when it is reached, are shown for each timescale and transient viscosity in Table 5.2.

Clearly, the maximum relative difference and the time at which it is observed are not heavily influenced by the timescale of the loading process, while they are determinant in the analysis of the transient viscosity.

5.1.2 Forebulge

An important parameter to determine the rheological behaviour of the upper mantle is the time of formation of the forebulge: by looking at Figures 5.1c, 5.1d, 5.3c, 5.3d, 5.5c, 5.5d, 5.7c and 5.7d, it can be seen that the forebulge, located at about 161°, is already

History	Model	Relative difference	Time (y)
0	1	17%	100
0	2	9.0%	400
1	1	15%	200
1	2	7.8%	950
10	1	15%	200
10	2	7.8%	750
100	1	15%	200
100	2	7.8%	750

Table 5.2: Radial maximum relative differences at the bottom of the subsided region. The table shows the differences $(u_r^i - u_r^0)/u_r^0$, where $i = 1, 2$, as shown in column 'Model'.

starting to form at the 1000 yr benchmark when a transient behaviour is implied, while at the same time it is not present when the upper mantle is modelled as a Maxwell fluid, as can be seen in Figures 5.1a, 5.3a, 5.5a and 5.7a.

In this region, the maximum relative difference is reached much later than inside the subsided region. This is due to the forebulge displacement of the Maxwell model approaching zero while the forebulge is already growing in the Burgers models. The values of the maximum relative displacement, together with the time at which it is reached, are shown in Table 5.3.

History	Model	Relative difference	Time (y)
0	1	1150%	1000
0	2	1214%	1000
1	1	107%	1000
1	2	104%	2000
10	1	600%	2000
10	2	528%	2000
100	1	601%	2000
100	2	528%	2000

Table 5.3: Radial maximum relative differences at the highest point of the forebulge. The table shows the differences $(u_r^i - u_r^0)/u_r^0$, where $i = 1, 2$, as shown in column 'Model'.

A similar study can be done in terms of latitude displacement. In this case, the behaviour is much more similar to that of the subsided region, as can be seen in Table 5.4. The relative difference in terms of latitude is much lower than the one analysed in terms of radial displacement, and it is reached within the first 1000 years. It does not strongly depend on the chosen time-history, so it can be used to easily distinguish between different transient viscosities.

History	Model	Relative difference	Time (y)
0	1	51%	100
0	2	23%	350
1	1	45%	200
1	2	20%	600
10	1	45%	200
10	2	20%	650
100	1	45%	200
100	2	20%	650

Table 5.4: Latitude maximum relative differences at the highest point of the forebulge. The table shows the differences $(u_\theta^i - u_\theta^0)/u_\theta^0$, where $i = 1, 2$, as shown in column 'Model'.

5.1.3 Local latitude displacement maximum

The point of maximum latitude displacement is located under the load, at a colatitude of about 168°, and behaves similarly to the latitude displacement on top of the forebulge or the radial displacement at the bottom of the subsided region, as can be seen in Table 5.5.

History	Model	Relative difference	Time (y)
0	1	53%	100
0	2	24%	300
1	1	46%	150
1	2	21%	550
10	1	46%	150
10	2	21%	600
100	1	46%	200
100	2	21%	600

Table 5.5: Latitude maximum relative differences at the point of highest latitude displacement. The table shows the differences $(u_\theta^i - u_\theta^0)/u_\theta^0$, where $i = 1, 2$, as shown in column 'Model'.

Chapter 6

Conclusions

In this work, it was deemed possible to develop a program that computes the surface displacement of a SVISG planet subject to AX loads by defining the load function, the time-history and the Love numbers by adapting TABOO's code. This program, SKAL, is able to use non-convoluted Love numbers in the time domain, as provided by TABOO, or convoluted Love numbers, like the ones provided by ALMA^3. This evidenced an average relative discrepancy of 3.5% between the displacement computed by TABOO and the one deduced from the Love numbers calculated by ALMA^3.

Concerning the effects of transient rheological models on glacial isostatic depression, the displacement difference between the transient models and a viscoelastic Maxwell rheology has been evaluated along a meridian, with three benchmark points taken as references: the lowest point of the subsided region, the highest point of the forebulge, and a point of maximum latitude displacement.

Since this work aims at finding rheology-dependent quantities, four different time-histories have been considered: a step loading and simple loadings with three timescales. The analysis of the relative displacement difference at the three benchmark points showed that its maximum values and the times at which they are reached are particularly useful for determining the transient viscosity, since they depend only slightly on the time history, while they are strongly dependent on the rheological model. The characteristic times of glacial isostasy have a magnitude of 10–100 kyr, but the effects of the considered transient rheologies can already be observed with a simple loading lasting only 1 kyr, since the characteristic times of the models have a magnitude of 0.01–1 kyr. With the step loading, which cannot be used to model glacial isostatic phenomena, the above-mentioned quantities assume different values, as expected.

The choice of a transient rheology yields its most evident effects in the first thousands of years after the beginning of the loading process. In the first millennium after the beginning of the process, using transient viscosity values one order of magnitude lower than or equal to the steady-state viscosity causes an average relative displacement increase of about 10% when compared to a Maxwell rheology. A particularly evident effect of the transient behaviour is the anticipation of the development of a forebulge.

Excluding the step time-history, the analysis of latitude displacement showed similar results both on top of the forebulge and at a colatitude of 168°. In model 1, where the transient viscosity is one tenth of the steady state viscosity, the highest relative difference from the Maxwell model is reached after 150–200 yr, and takes on a value of 45–46%. In model 2, where the transient viscosity is the same as the steady-state viscosity, the maximum relative difference is reached later, after 550–650 yr, with a lower value of 20–21%. The analysis of the radial displacement under the load axis yields similar results: model 1 reaches the maximum relative difference of 15% after 200 yr, while model 2 reaches the maximum value of 7.8% after 750–950 yr.

On top of the forebulge, the maximum relative difference in terms of radial displacement is reached later, between 1000 and 2000 years after the beginning of the load, and it reaches much higher values. This high relative difference, however, is only due to the low radial displacement, since the peripheral region starts with negative radial displacement but later assumes positive displacement values.

Appendix A

Derivation of Burgers constitutive equations

To obtain the constitutive equation for a Burgers model using a series of Maxwell and Kelvin-Voigt elements, as shown in Figure 2.3, we must sum the first and second derivatives of the strain tensor, multiplied, respectively, by the elastic modulus and the viscosity of the Kelvin-Voigt element; these quantities are shown in Eqs. (A.1) and (A.2):

$$E_{KV}\dot{\varepsilon} = E_{KV}\dot{\varepsilon}_{KV} + E_{KV}\dot{\varepsilon}_{M} = E_{KV}\dot{\varepsilon}_{KV} + \frac{E_{KV}}{E_M}\dot{\sigma} + \frac{E_{KV}}{\eta_M}\sigma\,, \tag{A.1}$$

$$\eta_{KV}\ddot{\varepsilon} = \eta_{KV}\ddot{\varepsilon}_{KV} + \eta_{KV}\ddot{\varepsilon}_{M} = \eta_{KV}\ddot{\varepsilon}_{KV} + \frac{\eta_{KV}}{E_M}\ddot{\sigma} + \frac{\eta_{KV}}{\eta_M}\dot{\sigma}\,. \tag{A.2}$$

Given the constitutive law expressed by Eq.(2.21) for a Kelvin-Voigt material, the sum of the quantities defined in Eqs. (A.1) and (A.2) yields:

$$E_{KV}\dot{\varepsilon} + \eta_{KV}\ddot{\varepsilon} = \frac{E_{KV}}{\eta_M}\sigma + \left(1 + \frac{E_{KV}}{E_M} + \frac{\eta_{KV}}{\eta_M}\right)\dot{\sigma} + \frac{\eta_{KV}}{E_M}\ddot{\sigma}\,. \tag{A.3}$$

The coefficients of this relation can be rearranged to obtain Eq. (2.24).

When the Burgers material is described as a generalized Maxwell model, as shown in Figure 2.4, the constitutive equation can be derived using either the Laplace transform or the following differential operators:

$$T_i = \frac{d}{dt} + \frac{E_i}{\eta_i}\,, \tag{A.4}$$

where $i = 1, 2$. Given one of the two branches of the generalized Maxwell model, its constitutive equation can thus be written as:

$$E_i\dot{\varepsilon} = T_i\sigma_i\,. \tag{A.5}$$

The constitutive equation can be obtained by adding the two quantities defined by the following equation (A.6):

$$(1-\delta_{ij})\, T_i E_j \dot{\varepsilon} = (1-\delta_{ij})\, T_i T_j \sigma_j \,. \tag{A.6}$$

Since the two operators commute, this leads to

$$(T_2 E_1 + T_1 E_2)\, \dot{\varepsilon} = T_1 T_2 \left(\sigma_1 + \sigma_2\right). \tag{A.7}$$

The total stress is the sum of the stresses of the two branches; thus, by expanding the operators, we obtain the following constitutive equation:

$$(E_1 + E_2)\, \ddot{\varepsilon} + E_1 E_2 \left(\frac{1}{\eta_1} + \frac{1}{\eta_2}\right) \dot{\varepsilon} = \ddot{\sigma} + \left(\frac{E_1}{\eta_1} + \frac{E_2}{\eta_2}\right) \dot{\sigma} + \frac{E_1 E_2}{\eta_1 \eta_2} \sigma \,. \tag{A.8}$$

Rearranging the coefficients, we obtain Eq. (2.25).

Appendix B

Implementation and testing of SKAL

The development of SKAL was supported by the usage of generative artificial intelligence, specifically Claude 4.6 Sonnet (released on 17 February 2026), from May to June 2026.

AI was mainly used to easily navigate TABOO's code and extract the required functions and variables. The configuration function has also been written with the help of AI starting from the configuration functions of TABOO and ALMA^3. For this reason, SKAL has been made able to accept non-convoluted Love numbers in the time domain, which are part of TABOO's outputs, and convolute them internally, as a method to test the correctness of the displacement calculation function. As expected, the results were identical to those provided by TABOO.

SKAL was later used in conjunction with ALMA^3 and the results were compared with TABOO's outputs, as described in section 4.2.

References

Boughanemi, A. and Mémin, A. (Sept. 2024). 'Effects of Andrade and Burgers rheologies on glacial isostatic adjustment modeling in Antarctica'. In: *Geodesy and Geodynamics* 15.5, pp. 429–440. DOI: 10.1016/j.geog.2023.12.008.

Brandes, C., Steffen, H., Steffen, R., Li, T. and Wu, P. (Sept. 2025). 'Effects of the Last Quaternary Glacial Forebulge on Vertical Land Movement, Sea-Level Change, and Lithospheric Stresses'. In: *Reviews of Geophysics* 63.3. DOI: 10.1029/2024RG000852.

Cathles, L. M. (1975). *Viscosity of the Earth's Mantle*. Princeton Legacy Library. Princeton, US: Princeton University Press. ISBN: 978-0-691-64492-9. DOI: 10.1515/9781400867684.

Dziewonski, A. M. and Anderson, D. L. (June 1981). 'Preliminary reference Earth model'. In: *Physics of the Earth and Planetary Interiors* 25.4, pp. 297–356. DOI: 10.1016/0031-9201(81)90046-7.

Karato, S. (July 2010). 'Rheology of the Earth's mantle: A historical review'. In: *Gondwana Research* 18.1, pp. 17–45. DOI: 10.1016/j.gr.2010.03.004.

Melini, D., Saliby, C. and Spada, G. (Dec. 2022). 'On computing viscoelastic Love numbers for general planetary models: the ALMA3 code'. In: *Geophysical Journal International* 231.3, pp. 1502–1517. DOI: 10.1093/gji/ggac263.

Müller, G. (Dec. 1986). 'Generalized Maxwell bodies and estimates of mantle viscosity'. In: *Geophysical Journal International* 87.3, pp. 1113–1141. DOI: 10.1111/j.1365-246X.1986.tb01986.x.

Pan, L., Mitrovica, J. X., Milne, G. A., Hoggard, M. J. and Woodroffe, S. A. (May 2024). 'Timescales of glacial isostatic adjustment in Greenland: is transient rheology required?' In: *Geophysical Journal International* 237.2, pp. 989–995. DOI: 10.1093/gji/ggae095.

Peltier, W. R., Yuen, D. A. and Wu, P. (Oct. 1980). 'Postglacial rebound and transient rheology'. In: *Geophysical Research Letters* 7.10, pp. 733–736. DOI: 10.1029/GL007i010p00733.

Pollitz, F. F. (Oct. 2003). 'Transient rheology of the uppermost mantle beneath the Mojave Desert, California'. In: *Earth and Planetary Science Letters* 215.1–2, pp. 89–104. DOI: 10.1016/S0012-821X(03)00432-1.

Sabadini, R., Piersanti, A. and Spada, G. (Apr. 1995). 'Toroidal/poloidal partitioning of global post-seismic deformation'. In: *Geophysical Research Letters* 22.8, pp. 985–988. DOI: 10.1029/95GL00819.

Spada, G. (Oct. 2003). *The theory behind TABOO*. https://github.com/danielemelini/TABOO/blob/master/DOC/TABOO-theory.pdf. Accessed: 2026-08-29.

Spada, G. (Feb. 2005). *TABOO User guide*. https://github.com/danielemelini/TABOO/blob/master/DOC/TABOO_User_Guide.pdf. Accessed: 2026-08-29.

Spada, G. and Melini, D. (2025). *Glacial Isostatic Adjustment: Theory for a Spherically Symmetric Earth and Numerical Results*. Springer Geophysics. Cham, CH: Springer. ISBN: 978-3-031-90538-4. DOI: 10.1007/978-3-031-90538-4.

Tschoegl, N. W. (1989). *The Phenomenological Theory of Linear Viscoelastic Behavior: An Introduction*. Springer Geophysics. Berlin Heidelberg, DE: Springer-Verlag. ISBN: 978-3-642-73602-5. DOI: 10.1007/978-3-642-73602-5.

Whitehouse, P. L. (2018). 'Glacial isostatic adjustment modelling: historical perspectives, recent advances, and future directions'. In: *Earth Surface Dynamics* 6.2, pp. 401–429. DOI: 10.5194/esurf-6-401-2018.